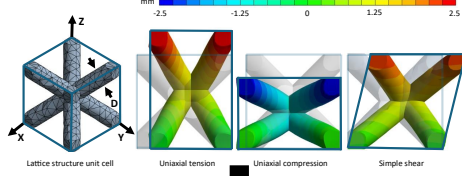
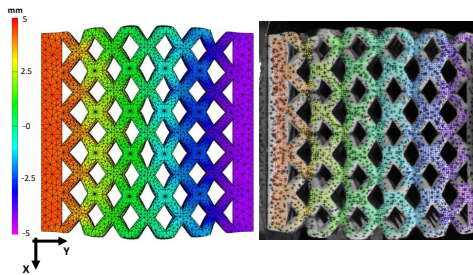


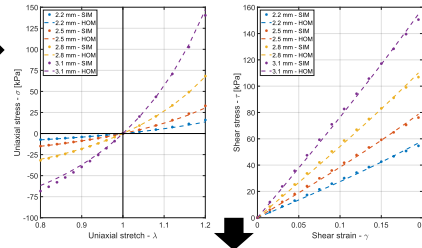
### Analysis of the effective unit cell behavior using FE simulations



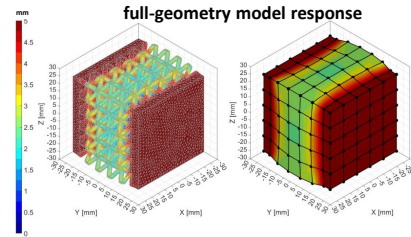
### Evaluation of FE simulation accuracy against experimental measurements



### Homogenization by fitting Fung hyperelastic orthotropic constitutive parameters



### Comparison between homogenized and full-geometry model response



## Graphical Abstract

### Soft orthotropic hyperelastic lattice structures: numerical homogenization and experimental validation

Dror Raf, Itay Magen, Amit Ashkenazi, Lee Jordan, Dana Solav

## Highlights

### **Soft orthotropic hyperelastic lattice structures: numerical homogenization and experimental validation**

Dror Raf, Itay Magen, Amit Ashkenazi, Lee Jordan, Dana Solav

- Homogenization of thick-beamed orthotropic lattice structures under finite deformations.
- Fung hyperelastic orthotropic constitutive parameters are fitted for tension, compression, and shear.
- Experiments are conducted on cubic lattice structures fabricated from TPU using SLS.
- Homogenization results agree well with full structure simulations and experiments.
- Simulation time is reduced by two to three orders of magnitude.

# Soft orthotropic hyperelastic lattice structures: numerical homogenization and experimental validation

Dror Raf<sup>a</sup>, Itay Magen<sup>a</sup>, Amit Ashkenazi<sup>a</sup>, Lee Jordan<sup>a</sup>, Dana Solav<sup>a</sup>

<sup>a</sup>*Faculty of Mechanical Engineering, Technion, Haifa, 320003, Israel*

---

## Abstract

Lattice structures have become increasingly popular in various applications due to their lightweight and wide range of effective properties that can be locally tailored by adjusting their geometric features. Finite element (FE) simulations are commonly used to predict their mechanical response and inform inverse design algorithms. However, these simulations pose significant computational demands due to the large number of elements needed for meshing lattice geometries. This challenge can be addressed by replacing lattice geometries with a homogeneous solid of equivalent mechanical properties, a process known as homogenization. However, determining a suitable constitutive model and parameters is difficult, particularly when the response is nonlinear and anisotropic. To this end, this study presents a method for numerically homogenizing orthotropic lattice structures subjected to large elastic deformations. FE simulations of lattice unit cells are employed to quantify their nonlinear elastic response under large uniaxial tension, compression, and simple shear deformations. The simulation results are then used to fit the constitutive model parameters for the effective behavior of the unit cells, employing a Fung orthotropic hyperelastic formulation. The proposed homogenization method is validated through comparisons with full-geometry simulations and compression experiments on beam-based cubic lattice structures manufactured from thermoplastic polyurethane (TPU) using selective laser sintering (SLS). Furthermore, we compare the response of a beam with orthotropic unit cells under bending, which activates multiple deformation modes. The results demonstrate the feasibility and computational efficiency of the proposed homogenization method, highlighting the potential of this approach for efficient modeling and design of lattice structures in engineering applications.

*Keywords:* Additive manufacturing (AM), digital image correlation (DIC), finite element analysis (FEA), metamaterials, multiscale modeling, selective laser sintering (SLS), thermoplastic polyurethane (TPU)

---

## 1. Introduction

Additive manufacturing (AM) technologies offer new opportunities to fabricate porous structures with complex shapes and topologies that are difficult or impossible to achieve with conventional manufacturing methods, allowing unprecedented flexibility in design and fabrication across various applications and fields [1, 2]. In particular, in the field of biomechanics, AM has opened up possibilities for fabricating data-driven patient-specific devices with locally variable mechanical properties aimed at adjusting the loads transferred to the body through the device. Examples include shoe midsoles [3, 4], insoles [5, 6], prosthetic sockets [7, 8], and wheelchair

9 cushions [9]. By locally adjusting topological and geometrical parameters within the structure,  
10 we can tune its macro-scale effective mechanical properties. This allows us to create interfaces  
11 with varying properties in different regions, thereby substantially expanding the range of avail-  
12 able properties compared to merely combining different solid materials.

13 The computer-aided design (CAD) of devices like these is typically informed by mechan-  
14 ical numerical simulations, such as the finite element (FE) method, often involving multiple  
15 iterations aimed at optimizing the desired mechanical response. However, simulating lattice ge-  
16 ometries poses significant computational demands due to the large number of elements needed  
17 to mesh them. This problem becomes particularly challenging when a large set of iterative simu-  
18 lations is required in the design process. This challenge can be addressed by replacing the lattice  
19 geometry with a homogeneous solid material that has equivalent effective mechanical properties,  
20 in a process known as homogenization (e.g., [10, 11, 12]). The goal of this process is to find  
21 the parameters of a suitable constitutive law of a solid material, such that it will respond to loads  
22 similarly to the lattice structure, as illustrated in the example shown in Figure 1.

23 Several methods for homogenization of lattice structures are described in the literature. The  
24 beam theory approach has been employed to derive the effective stiffness of various lattice unit  
25 cells. The Euler–Bernoulli beam theory was introduced in the seminal paper by Gibson and  
26 Ashby (1982) to analytically derive the closed-form expression for the effective modulus of cel-  
27 lular materials [13]. This approach has been further developed in numerous studies since then  
28 [14]. This approach is limited by thin beam and small strain assumptions. Timoshenko beam  
29 theory has been employed to address some of these limitations by including shear deformation,  
30 making it suitable for moderately thick beams as well. However, for thick-beam lattice structures,  
31 Timoshenko theory also has several limitations that stem from its assumptions of a uniform shear  
32 strain over the beam cross-section, and exclusion of higher-order effects and various boundary  
33 and local effects [15]. To computationally obtain the effective homogeneous material parameters  
34 of a unit cell, periodic boundary conditions (PBCs) are applied to ensure that deformation fields  
35 are periodic across cell boundaries, mimicking an infinite periodic medium. Typically, FE simu-  
36 lations are used to evaluate the response of a unit cell to desirable loads. The extraction of equiv-  
37 alent homogeneous material parameters from the results of these simulations can be achieved by  
38 means of the strain energy method [16, 17], or by averaging the stress-strain response across the  
39 unit cell’s volume [18, 10], which is the method adopted in the current research.

40 To date, most research on 3D-printed lattice structures has primarily focused on lightweight,  
41 minimum-compliance structures, which are typically made of relatively stiff materials that ex-  
42 hibit inelastic behavior under large deformations. Consequently, the majority of modeling and  
43 simulation studies, along with commercial CAD tools, have focused their elastic analysis within  
44 the linear regime [19, 20, 21, 22, 23, 24, 25, 26, 27, 28].

45 Recently, there has been increasing interest in the design and fabrication of soft lattice struc-  
46 tures and metamaterials that can undergo large (nonlinear) elastic deformations (e.g., [29, 30]).  
47 Homogenization of these structures is challenging due to the complexity of constitutive models  
48 required to effectively capture their nonlinear response. Some studies limited their analysis to  
49 2D lattice metamaterials or in-plane response (e.g., [31, 32, 33, 34]).

50 Recent advances in the homogenization of 3D lattice structures focused on truss-like struc-  
51 tures with slender beams (e.g., [12, 35, 36]). Although this approach simplifies the simulations  
52 and reduces computational costs, it is not applicable to unit cells with thick beams, which are the  
53 primary focus of this study. Moreover, in many cases, the homogenization did not account for  
54 both anisotropy and nonlinear elasticity. For example, Jamshidian et al. (2020) [36] presented  
55 a multiscale approach using FE simulations with beam elements to evaluate the effective behav-

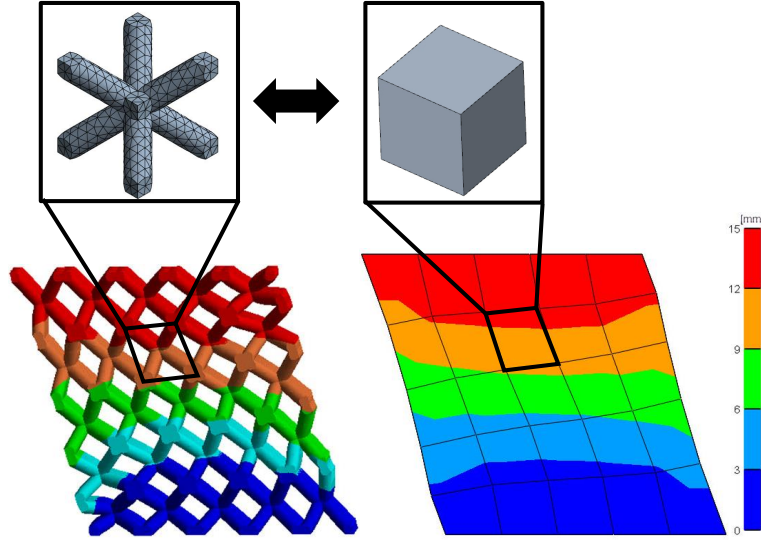


Figure 1: Example of computational homogenization concept: FE simulations of the full lattice structure with numerous elements (left) and of its corresponding homogenized solid model with few elements, exhibiting comparable responses under simple shear, as demonstrated by their horizontal displacements.

ior of lattice structures under large uniaxial deformations, focusing on the buckling response, and homogenizing to a Hyperfoam *isotropic* constitutive model. Other studies that homogenized the anisotropic response of lattice structures limited their analysis to the linear elastic regime (e.g., [37, 21]). Shojaee et al. (2024) [38] proposed a homogenization technique for *shell* lattice structures, by fitting their anisotropic linear elastic response using a physics-augmented neural network model. However, a gap remains in establishing a comprehensive framework that captures the full anisotropic and nonlinear elastic behavior of 3D lattice structures with thick-beam unit cells under multiaxial finite deformations.

To the best of our knowledge, this is the first study presenting the numerical homogenization of a hyperelastic orthotropic constitutive model for thick-beam lattice structures subjected to finite multiaxial deformations. We employ the Fung compressible orthotropic hyperelastic constitutive model to homogenize the response of the structures to uniaxial tension, uniaxial compression, and simple shear. Both the Hyperfoam and the Fung models effectively capture the macro-scale compressibility of the structures. However, the Fung orthotropic model supplements the anisotropic behavior. We evaluate the accuracy of the method through comprehensive comparisons between the mechanical response (including reaction force and structure deformation) of simulated lattice structures and their homogenized solid counterparts, as well as between FE simulations and experimental results of lattice structures fabricated from thermoplastic polyurethane (TPU) using selective laser sintering (SLS).

## 2. Materials and Methods

The research methodology combines a homogenization framework, experimental testing, and FE simulations, organized as follows: [subsection 2.1](#) presents the mechanical characterization of

78 the constituent material, which is used as input for all the full-geometry lattice structure sim-  
79 ulations. [subsection 2.2](#) introduces the homogenization procedure, including the PBCs in ten-  
80 sion, compression, and shear. It also describes the homogeneous Fung constitutive model and  
81 its model parameters, detailing the FE simulations of unit cells and the process of fitting the  
82 Fung model parameters to the simulation results. Then, [subsection 2.3](#) outlines the experimental  
83 methods used to analyze the behavior of body-centered (BC) cubic lattice structures under com-  
84 pression. [subsection 2.4](#) presents the FE simulations corresponding to the experiments, including  
85 a demonstrative FE simulation case of a beam with orthotropic lattice cells under a distributed  
86 force that causes bending. This case is designed to test the effectiveness of homogenization in  
87 situations involving multiple deformation modes. Additionally, it describes the procedure used  
88 to evaluate the accuracy of the homogenized models by considering both reaction forces and 3D  
89 deformations.

### 90 2.1. Characterization of the mechanical properties of the constituent material

91 The lattice structures used in this research were 3D printed using an SLS printer (Lisa Pro,  
92 Sinterit, Warsaw, Poland) from a Flexa Bright™ TPU powder (Sinterit, Warsaw, Poland). In a  
93 previous study [39], we characterized the mechanical properties of this material through uniaxial  
94 tension and compression tests on specimens printed in multiple orientations. The experiments  
95 included pre-conditioning cycles, measurement of stress relaxation, and the estimation of equi-  
96 librium force using exponential decay fitting. Full-field strains were measured using 3D digital  
97 image correlation (3D-DIC), and micro-computed tomography (micro-CT) scans were employed  
98 to accurately determine the specimens' cross-sectional areas. The results indicate an approxi-  
99 mately linear equilibrium stress-strain relationship up to strains of  $\sim \pm 20\%$ . However, stiffness  
100 varied with printing orientation and between tension and compression. In the current study, we  
101 model the material as isotropic linear elastic, a deliberate compromise that balances model fi-  
102 delity and simplicity. Since different parts in the lattice structures may experience both tension  
103 and compression, and are printed in multiple orientations within the same structure, we adopted  
104 the average values for the Young's modulus and Poisson ratio obtained from the previous study  
105 [39], namely  $E = 19.8$  MPa and  $\nu = 0.41$ , respectively.

### 106 2.2. Homogenization framework

#### 107 Homogenization with periodic boundary conditions (PBCs)

108 PBCs are employed to characterize a unit cell's effective mechanical response by applying  
109 finite deformations under various loading modes, including uniaxial tension, uniaxial compres-  
110 sion, and simple shear, to extract the unit cell's effective homogenized response.

111 The finite deformation gradient tensor is defined as  $\mathbf{F} = \partial \mathbf{x} / \partial \mathbf{X}$ , where  $\mathbf{X}$  denotes the posi-  
112 tion vector of a material point in the undeformed (reference) configuration, and  $\mathbf{x}$  represents the  
113 corresponding position vector in the deformed (current) configuration. For uniaxial tension and  
114 compression tests  $\mathbf{F}$  takes the form

$$\mathbf{F} = \begin{bmatrix} \lambda_x & 0 & 0 \\ 0 & \lambda_y & 0 \\ 0 & 0 & \lambda_z \end{bmatrix} \quad (1)$$

115 where  $\lambda_x, \lambda_y, \lambda_z$  are the stretches along the X, Y, and Z axes, respectively. Each stretch is  
116 defined as  $\lambda_i = 1 + \Delta_i / L_i$ , where  $\Delta_i$  and  $L_i$  are the nominal elongation and the initial length of the  
117 unit cell in the  $i^{\text{th}}$  direction, respectively.

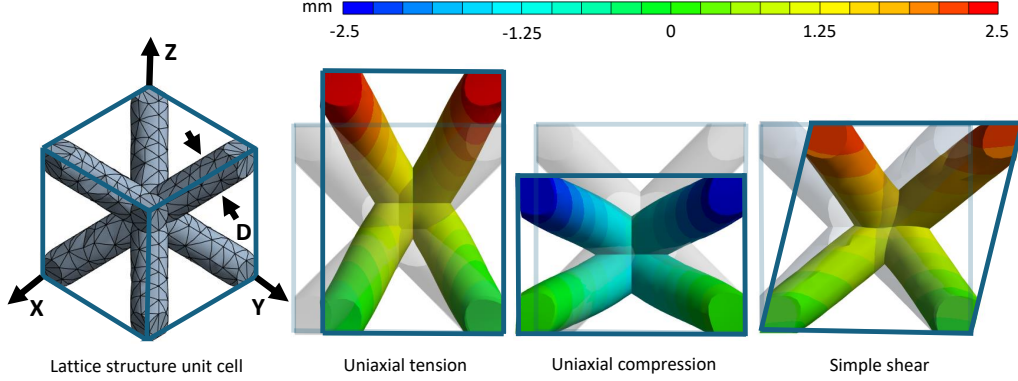


Figure 2: Deformation modes of BC lattice Unit cell. From left to right: The geometry of a BC unit cell with a beam diameter ( $D$ ) is enclosed by a volume bounding box. The FE Simulation results display the displacement fields for uniaxial tension and compression (indicated by positive and negative vertical displacements, respectively), as well as simple shear (represented by horizontal displacement).

118 For a simple shear test, the deformation gradient tensors are

$$\mathbf{F}_{xy} = \begin{bmatrix} 1 & \gamma_{xy} & 0 \\ 0 & 1 & 0 \\ 0 & 0 & 1 \end{bmatrix}, \mathbf{F}_{xz} = \begin{bmatrix} 1 & 0 & \gamma_{xz} \\ 0 & 1 & 0 \\ 0 & 0 & 1 \end{bmatrix}, \mathbf{F}_{zy} = \begin{bmatrix} 1 & 0 & 0 \\ 0 & 1 & 0 \\ 0 & \gamma_{zy} & 1 \end{bmatrix} \quad (2)$$

119 where  $\gamma_{xy}$ ,  $\gamma_{xz}$ , and  $\gamma_{zy}$  are the nominal shear strains in the shearing planes XY, XZ, and ZY,  
 120 respectively. The shear strains are defined as  $\gamma_{ij} = \Delta_i/L_j$ .

121 For applying the PBCs, we consider a generic orthotropic unit cell with three orthogonal  
 122 symmetry planes that align with the X, Y, and Z principal axes. The unit cell is wrapped by  
 123 a bounding box that represents the equivalent homogenized cell dimensions. A representative  
 124 bounding box and three deformation modes applied to a BC unit cell are depicted in Figure 2.

125 We define the nodes of the unit cell that coincide with the bounding box surfaces as the outer  
 126 main nodes, on which the PBCs are applied. There are six sets of such nodes, corresponding to  
 127 the six faces of the bounding box. Each face is identified by the outward-pointing unit normal  
 128 vector. Accordingly, the faces are denoted as  $U^x, U^y, U^z$  and  $U^{-x}, U^{-y}, U^{-z}$ , representing the  
 129 positive and negative directions along the X, Y, and Z axes, respectively. Each set of outer main  
 130 nodes has six degrees of freedom (DOF): three translational DOFs ( $U_x, U_y, U_z$ ) along the X, Y,  
 131 and Z axes, and three rotational DOF ( $U_\varphi, U_\theta, U_\psi$ ) about the same axes. A PBC applied to nodes  
 132 on the  $i^{th}$  face and the  $j^{th}$  DOF is denoted as  $U_j^i$ .

133 For each simulation, we impose appropriate translational boundary conditions while leaving  
 134 the rotational DOFs unconstrained. In the uniaxial tension and compression tests, we apply  
 135 zero displacement conditions to  $U_x^{-x}, U_y^{-y}$ , and  $U_z^{-z}$ . Along the loading direction, denoted as  $k$   
 136 ( $k \in \{X, Y, Z\}$ ), a prescribed displacement  $\Delta_k$  is applied to  $U_k^k$ , while the DOFs in all transverse  
 137 directions remain free, as illustrated in Figure 3. In the simple shear test in direction  $km$  ( $k \neq m$ ,  
 138 with  $k, m \in \{X, Y, Z\}$ ), a zero displacement condition is enforced on  $U_n^{\pm n}$ , where  $n$  is the axis  
 139 normal to the  $k$ - $m$  plane. Additionally, zero displacement is applied to  $U_k^{-m}$  and  $U_m^m$ , while a  
 140 prescribed displacement  $\Delta_k$  is applied to  $U_k^m$ , as illustrated in Figure 3.

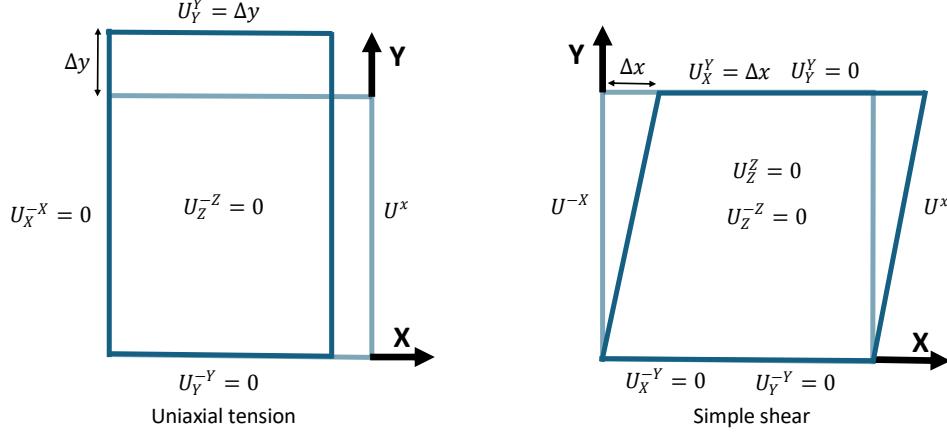


Figure 3: Schematic of PBC definitions. The notations for faces and PBCs are depicted for uniaxial tension along the  $Y$  direction (left), and for simple shear in the  $XY$  plane (right). The boundary conditions associated with the  $i^{\text{th}}$  face and the  $j^{\text{th}}$  DOF are denoted as  $U_j^i$ . Unless explicitly specified, all other DOFs remain unconstrained.

141 In order to evaluate the nonlinear response of the lattice structure, we prescribed 10 equally  
 142 spaced displacement steps. At each displacement step, we record the simulated displacement of  
 143 the transverse directions and the volume change of the bounding box. Additionally, we compute  
 144 the simulated volumetric average stress tensor of every element and calculate the volumetric  
 145 average stress of the simulated model as:

$$\sigma_{avg}^N = \frac{\sum_{i=1}^m v_i \sigma_i}{\sum_{i=1}^m v_i} \quad (3)$$

146 where  $m$  is number of elements in the model,  $v_i$  and  $\sigma_i$  are the volume and stress of the  $i^{\text{th}}$   
 147 element, and  $N$  is the displacement step.

148 The volume ratio of the unit cell (UC) and the bounding box (BB) is defined by:

$$\beta = \frac{V_{UC}^N}{V_{BB}^N} \quad (4)$$

149 where  $V_{UC}^N = \sum_{i=1}^m v_i$  and  $V_{BB}^N = V_{BB}^0 \lambda_x^N \lambda_y^N \lambda_z^N$ .

150 Multiplying (3) with (4) yields the stress tensor of the homogenized unit cell:

$$\sigma_{BB}^N = \beta \sigma_{avg}^N \quad (5)$$

### 151 *Constitutive model for the homogeneous material*

152 To model the large elastic deformations in soft lattice structures, hyperelastic constitutive  
 153 models are employed to provide closed-form relations between effective stress and deforma-  
 154 tion. Among the models evaluated, the Fung orthotropic compressible hyperelastic model [40]  
 155 appeared suitable for capturing both the uniaxial and the shear loading conditions.

156 The strain energy density (SED) function  $\Psi$  for this model can be written as:

$$\Psi = \frac{c_0}{2} \left[ e^Q - 1 \right] + \frac{K}{2} (\ln(J))^2 \quad (6)$$

157 where the Jacobian  $J = \det[\mathbf{F}]$  represents the dilatation, and the scalar variable  $Q$  for orthotropic  
 158 symmetries is given by:

$$Q = c_0^{-1} \sum_{i=1}^3 \left[ 2\mu_i \mathbf{M}_i : \mathbf{E}^2 + \sum_{j=1}^3 \lambda_{ij} (\mathbf{M}_i : \mathbf{E}) (\mathbf{M}_j : \mathbf{E}) \right] \quad (7)$$

159 In (7),  $:$  denotes a tensorial inner product, the second-order tensor  $\mathbf{M}_i$  is defined by  $\mathbf{M}_i = \mathbf{V}_i \otimes \mathbf{V}_i$ ,  
 160 where  $\otimes$  is the outer product and  $\mathbf{V}_i$  is the initial direction of material axis  $i$  (in the orthotropic  
 161 case, there are three orthogonal material axes).  $\mathbf{E} = (\mathbf{F}^T \mathbf{F} - \mathbf{I})/2$  is the Green-Lagrange strain  
 162 tensor, where  $\mathbf{I}$  is the identity tensor.  $c_0$ ,  $\kappa$  and the orthotropic Lamé parameters  $\mu_i$  and  $\lambda_{ij}$  are  
 163 material parameters. The latter two are related to the Young's moduli  $E_i$ , shear moduli  $G_{ij}$  and  
 164 Poisson's ratios  $\nu_{ij}$  via

$$\begin{bmatrix} \lambda_{11} + 2\mu_1 & \lambda_{12} & \lambda_{13} & 0 & 0 & 0 \\ \lambda_{12} & \lambda_{22} + 2\mu_2 & \lambda_{23} & 0 & 0 & 0 \\ \lambda_{13} & \lambda_{23} & \lambda_{33} + 2\mu_3 & 0 & 0 & 0 \\ 0 & 0 & 0 & \frac{1}{2}(\mu_1 + \mu_2) & 0 & 0 \\ 0 & 0 & 0 & 0 & \frac{1}{2}(\mu_2 + \mu_3) & 0 \\ 0 & 0 & 0 & 0 & 0 & \frac{1}{2}(\mu_1 + \mu_3) \end{bmatrix}^{-1} = \begin{bmatrix} \frac{1}{E_1} & -\frac{\nu_{12}}{E_1} & -\frac{\nu_{13}}{E_1} & 0 & 0 & 0 \\ -\frac{\nu_{21}}{E_2} & \frac{1}{E_2} & -\frac{\nu_{23}}{E_2} & 0 & 0 & 0 \\ -\frac{\nu_{31}}{E_3} & -\frac{\nu_{32}}{E_3} & \frac{1}{E_3} & 0 & 0 & 0 \\ 0 & 0 & 0 & \frac{1}{G_{12}} & 0 & 0 \\ 0 & 0 & 0 & 0 & \frac{1}{G_{23}} & 0 \\ 0 & 0 & 0 & 0 & 0 & \frac{1}{G_{31}} \end{bmatrix} \quad (8)$$

165 In case the orthotropic material axes coincide with the  $X, Y, Z$  axes,  $Q$  is expressed as:

$$Q = c_0^{-1} (c_1 E_{11}^2 + c_2 E_{22}^2 + c_3 E_{33}^2 + 2c_4 E_{11} E_{22} + 2c_5 E_{22} E_{33} + 2c_6 E_{23} E_{33} + c_7 (E_{12}^2 + E_{21}^2) + c_8 (E_{23}^2 + E_{32}^2) + c_9 (E_{31}^2 + E_{13}^2)) \quad (9)$$

166 where  $E_{ij}$  are components of  $\mathbf{E}$  and the material parameters  $c_i$  ( $i = 1 \dots 9$ ) are related to the or-  
 167 thotropic Lamé parameters by [41]:

$$\begin{aligned} c_1 &= \lambda_{11} + 2\mu_1 \\ c_2 &= \lambda_{22} + 2\mu_2 \\ c_3 &= \lambda_{33} + 2\mu_3 \\ c_4 &= \lambda_{12} \\ c_5 &= \lambda_{23} \\ c_6 &= \lambda_{13} \\ c_7 &= \mu_1 + \mu_2 \\ c_8 &= \mu_2 + \mu_3 \\ c_9 &= \mu_3 + \mu_1 \end{aligned} \quad (10)$$

168 Consequently, the Fung model SED yields the Cauchy stress tensor  $\sigma$ :

$$\sigma = \frac{c_0}{2} J^{-1} e^{\mathcal{Q}} \mathbf{F} \frac{\partial \mathcal{Q}}{\partial \mathbf{E}} \mathbf{F}^T + \kappa \frac{\ln(J)}{J} \quad (11)$$

169 In the uniaxial case, using (1), (9) and (11) yields the stress components in the principal  
170 directions:

$$\begin{aligned} \sigma_{11} &= e^{\mathcal{Q}} \frac{\lambda_1}{\lambda_2 \lambda_3} (c_1 E_{11} + c_4 E_{22} + c_6 E_{33}) + \kappa \frac{\ln(J)}{J} \\ \sigma_{22} &= e^{\mathcal{Q}} \frac{\lambda_2}{\lambda_1 \lambda_3} (c_2 E_{22} + c_4 E_{11} + c_5 E_{33}) + \kappa \frac{\ln(J)}{J} \\ \sigma_{33} &= e^{\mathcal{Q}} \frac{\lambda_3}{\lambda_1 \lambda_2} (c_3 E_{33} + c_5 E_{22} + c_6 E_{11}) + \kappa \frac{\ln(J)}{J} \end{aligned} \quad (12)$$

171 In the simple shear case, using (2), (9) and (11) yields the stresses:

$$\begin{aligned} \sigma_{12} &= e^{\mathcal{Q}} \left( \frac{c_7 \gamma_{12}}{2} + \frac{c_2 \gamma_{12}^3}{2} \right) \\ \sigma_{13} &= e^{\mathcal{Q}} \left( \frac{c_9 \gamma_{13}}{2} + \frac{c_3 \gamma_{13}^3}{2} \right) \\ \sigma_{23} &= e^{\mathcal{Q}} \left( \frac{c_8 \gamma_{23}}{2} + \frac{c_2 \gamma_{23}^3}{2} \right) \end{aligned} \quad (13)$$

172 Since the geometry of the selected lattice unit cell has three perpendicular symmetry planes,  
173 the mechanical response of the structures is orthotropic. If all three planes are identical, the  
174 anisotropic model is reduced to cubic.

#### 175 *Finite Element simulation framework*

176 The unit cells were modeled using the Lattice feature in Creo Parametric 8.0 (PTC, Inc.,  
177 Boston, MA, USA), using a "star" configuration composed of beams with a circular cross-  
178 section, without corner fillets, as shown in Figure 2. Four BC cubic unit cells of size  $10 \times 10 \times$   
179  $10 \text{ mm}^3$  each were designed with different beam diameters:  $2.2 \text{ mm}$ ,  $2.5 \text{ mm}$ ,  $2.8 \text{ mm}$ ,  $3.1 \text{ mm}$ ,  
180 as well as one BC orthotropic unit cell of size  $15 \times 20 \times 17 \text{ mm}^3$  in the X, Y, and Z directions,  
181 respectively, and a uniform beam diameter  $D = 3.5 \text{ mm}$ .

182 FE simulations of the unit cells were conducted using ANSYS Mechanical 2023 R2 (AN-  
183 SYS, Inc., Canonsburg, PA, USA). The constituent material parameters were set to an isotropic  
184 linear elastic model with the parameters estimated for the Flexa Bright™ TPU, as described in  
185 subsection 2.1. The unit cells were meshed with quadratic 20-node hexahedral elements (type  
186 SOLID186 in Ansys). A mesh convergence study was conducted to select a mesh that balances  
187 between accuracy and computational time. The PBCs for tension, compression, and shear were  
188 employed as described above. Stress–stretch data obtained from the lattice unit cell simulations  
189 were used to determine the parameters of the Fung constitutive model by numerically solving the  
190 nonlinear sets of equations (12) and (13). A custom MATLAB R2024a code (The Mathworks  
191 Inc., Natick, MA, USA), using the *lsqcurvefit* function, was employed to estimate the optimal  
192 set of parameters that minimize the least-squares error between the model predictions and the  
193 simulation data. Each unit cell was subjected to uniaxial tension-compression stretch ( $\lambda$ ), and  
194 simple shear strain ( $\gamma$ ). For BC cubic cells, we used  $\lambda \in [0.8, 1.2]$  and  $\gamma \in [0, 0.2]$ , whereas for  
195 orthotropic cell the deformation ranges were  $\lambda \in [0.8, 1.4]$  and  $\gamma \in [0, 0.3]$ .

196 *2.3. Experiments on lattice structures*

197 *Compression experiments on cubic lattice structures*

198 Four lattice structures composed of  $5 \times 5 \times 5$  BC cubic unit cells with different beam diame-  
199 ters, as described in subsection 2.2, were designed. To the structures designed for fabrication, we  
200 added top and bottom solid plates of size  $50 \times 5 \times 50 \text{ mm}^3$  in the X, Y, and Z directions, respec-  
201 tively, each with a circular protrusion in the center, as shown in Figure 4a. The structures were  
202 processed with Sinterit Studio Advance printing slicer software (Sinterit, Warsaw, Poland). The  
203 same default printing parameters used for the TPU characterization experiments (subsection 2.1),  
204 including a layer height of 0.1 mm, were employed to generate the g-code for the printer. The  
205 structures were printed with the beam axes tilted  $45^\circ$  relative to the printing direction to minimize  
206 the variation in the beam dimensions within each lattice structure, as shown in Figure 4a.

207 The experiments were performed using a horizontal planar biaxial testing system (ADMET,  
208 Inc., Norwood, MA, USA) with a 2 kN load cell. The flat ends of the solid plates were glued  
209 to aluminum adapters that had a small circular recess to align with the circular protrusion of the  
210 structures on one side, and a circular recess to which the compression platens attach on the other  
211 side. The experimental setup configuration is shown in Figure 4c.

212 Since the constituent material exhibited softening during conditioning, a behavior commonly  
213 known as Mullin’s effect [42], we pre-conditioned the lattice structures by performing 10 cycles  
214 of 5 mm displacement compression on each side at a displacement rate of 0.25 mm/s, after which  
215 the force-displacement curve became stable. Next, we performed the compression tests with five  
216 equally spaced displacement steps. At each displacement step, the test was paused for 400 s,  
217 to allow for stress relaxation to occur and collect data for estimating the equilibrium force, as  
218 explained in subsection 2.3. During the pause in displacement, force measurements were taken  
219 every 1 s. The dimensions of the samples were measured before and after pre-conditioning, as  
220 well as before and after the tests, to assess whether any plastic deformations occurred.

221 *Measurement of lattice structures beam diameter*

222 Due to deviations in geometry between the CAD and printed structures, it was important to  
223 assess the actual dimensions of the printed lattice in order to construct FE simulations with the  
224 same dimensions. The density of the printed material was estimated by printing a solid cube and  
225 measuring its volume and weight. The beam diameter for each printed structure was estimated  
226 by weighing the structure and dividing the mass by the material’s density to calculate the volume.  
227 Then, the relationship between the beam diameter and the actual volume was established, and  
228 simulations were conducted on structures with the estimated beam diameters rather than the CAD  
229 ones.

230 *Experimental data processing*

231 The force at each constant displacement step is expected to exponentially decay and asymp-  
232 totically approach a constant value [43]. Therefore, for each displacement step, the correspond-  
233 ing equilibrium force was computed as the force predicted at infinite time, based on an exponen-  
234 tial decay model fitted to the available experimental data. We used MATLAB’s curve fitting tool  
235 (The Mathworks Inc., Natick, MA, USA) to fit the experimental force measurements to a general  
236 exponential function:

$$F(t) = \sum_{i=1}^N C_i e^{-k_i t} + F_\infty \quad (14)$$

237 where  $F(t)$  is the force value at time  $t$ ,  $N$  is the number of exponential terms,  $C_i$  is the amplitude  
238 of the  $i$  exponential term,  $k_i$  is the decay constant for each term, representing the rate at which the  
239 corresponding exponential terms decay, and  $F_\infty$  is the constant value that the force asymptotically  
240 approaches as  $t \rightarrow \infty$ , which is considered the equilibrium force.

241 To obtain accurate local displacement measurements during the tests, we utilized 3D-DIC, a  
242 non-contact optical method that provides full-field measurements. The 3D-DIC setup is shown  
243 in [Figure 4c](#) and consists of two Blackfly BFS-U3-51SM-C cameras (FLIR LLC, Wilsonville,  
244 OR, USA) featuring a 5-megapixel monochrome Sony IMX264 sensor, each equipped with a  
245 FUJINON HF25SA-1 lens with a focal length of 25 mm. The cameras were configured in a  
246 stereo arrangement and synchronized to capture simultaneous images of the test specimens at  
247 each displacement step. The images were acquired and stored using QS-GRABBER software  
248 (MatchID Nv, Gent, Belgium). One camera was positioned perpendicular to the specimen's  
249 measured surface, and the second was placed at a stereo angle of  $23^\circ$ . The standoff distance  
250 between the cameras and the specimen was 350 mm. The specimens were manually painted with  
251 a random speckle pattern of average size 2.5 mm using black ink, as shown in [Figure 4b](#).

252 The intrinsic and extrinsic parameters of the cameras were calibrated using a calibration  
253 target measuring  $9 \times 12$  cm with a grid of  $9 \times 12$  5 mm diameter dots, using the MatchID stereo  
254 calibration software. The images were processed using MatchID STEREO software to obtain  
255 full-field displacement maps, using the following processing parameters: a subset size of 21  
256 pixels, a step size of 10 pixels, an affine subset shape function, and Gaussian filtering with a  
257 kernel size of 5.

## 258 2.4. Simulations of full-geometry and homogenized lattice structures

### 259 *Compression FE simulations on cubic lattice structures*

260 Similarly to the simulations of the unit cells described in [subsection 2.2](#), FE simulations for  
261 the lattice structures were constructed using Ansys. FE simulations of the homogenized structure  
262 were conducted using FEBio version 4.4.0 [44], with GIBBON MATLAB toolbox version 3.5.0  
263 [45] for pre- and post-processing. The homogenized structure was meshed with 8-node trilinear  
264 hexahedral elements (hex8 in FEBio) of the corresponding unit cell size, and assigned the Fung  
265 model parameters (Fung-ortho-compressible in FEBio) obtained in the homogenization fitting  
266 process, while isotropic linear elastic model parameters (isotropic elastic in FEBio) estimated  
267 for the Flexa Bright™ TPU, as described in [subsection 2.1](#), assigned for the solid plates. All the  
268 simulations were performed using a Windows PC equipped with an Intel Core i7 CPU and 32  
269 GB RAM.

270 The boundary conditions for the simulations are illustrated in [Figure 5](#) for the simulations of  
271 the full-geometry lattice and the homogenized solid model. In all the simulations, displacements  
272 were prescribed in the  $\pm Y$  direction, and applied to the nodes located on the  $\pm Y$  boundaries  
273 (marked in blue in [Figure 5](#)), while the same nodes were fully constrained in the X and Z direc-  
274 tions. For SIM, the displacement values and the number of displacement steps were selected to  
275 match those measured during the experiments. The mesh and simulation results were imported  
276 from Ansys to MATLAB using *ANSYSimport* [46].

277 The key nodes (marked with red dots in [Figure 5](#)) are defined at the internal intersection points  
278 between adjacent lattice unit cells, located on the outer surface at the center of each junction  
279 where four diagonal struts meet. These nodes are used to evaluate the differences between the  
280 experimental and simulated results, as described in [subsection 2.4](#).

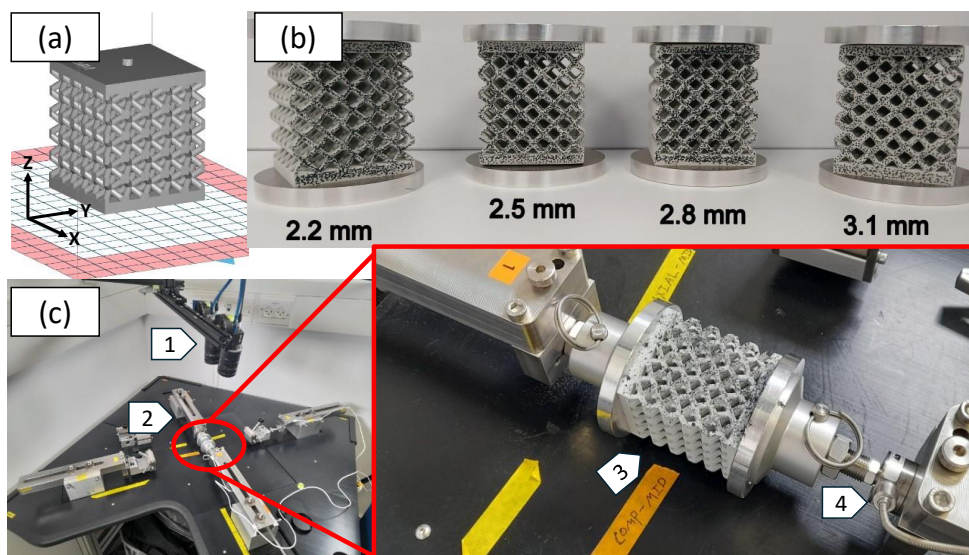


Figure 4: Lattice structures manufacturing and experimental setup: (a) Lattice structure CAD model in the printer's build volume showing the print orientation. The layers are built along the Z direction, and the printer's powder recoater moves along the Y direction. (b) SLS 3D-printed lattice structures with varying beam diameters. An aluminum adapter was adhesively bonded to each flat end of the structure to facilitate mounting in the compression test machine. (c) Experimental setup. (1) Two cameras in a stereo configuration. (2) Horizontal planar biaxial testing system. The inset on the right shows a zoomed-in view of the (3) lattice structure painted with a random speckle pattern mounted on the planar test machine grips, and (4) the 2 kN load cell.

281 *A demonstrative FE simulation with multiple deformation modes*

282 To evaluate the capability of our homogenization process to capture the mechanical response  
 283 in a more complex case, we designed a short beam with  $4 \times 10 \times 4$  orthotropic unit cells, each  
 284 with dimensions of  $15 \times 20 \times 17 \text{ mm}^3$  in the X, Y, and Z directions, respectively, and a uniform  
 285 beam diameter  $D = 3.5 \text{ mm}$ . The beam was subjected to a distributed force in the Z direction,  
 286 which was applied to all nodes on the upper surface, while all DOFs were fully constrained on  
 287 all nodes on the side surfaces, as illustrated in Figure 6. The force was linearly increased from  
 288 0 N to 300 N in 10 equally spaced steps. Similarly to the simulations of the cubic structures, two  
 289 equivalent FE simulations were constructed: the full lattice geometry simulated in Ansys, and a  
 290 homogenized simulation conducted in FEBio, using the homogenized parameters found through  
 291 the methods described in subsection 2.2.

292 *Evaluation of the accuracy of the homogenization process*

293 To evaluate the accuracy of the homogenization process, we compare both the reaction forces  
 294 and the displacements at key nodes. The displacement comparison between the homogenized  
 295 model and the full-geometry simulation includes all the key nodes. The comparison between  
 296 the full-geometry simulation and the experimental measurements is restricted to the key nodes  
 297 positioned in the central region, as illustrated in Figure 5. This is because some of the nodes  
 298 where the lattice structure is connected to the solid plate were obscured in the DIC images by  
 299 the platens of the testing machine. Moreover, although full-field measurements were captured on  
 300 the entire external upward-facing surface (as illustrated in Figure 13), only the values at the key  
 301 nodes were used for the quantitative comparison with the simulations [47].

302 To evaluate the quality of agreement between the experimental (EXP), simulation (SIM), and  
 303 homogenization (HOM) reaction force results, the normalized force differences are defined by:

$$\Delta F_{\text{tot}}^{\text{EXP-SIM}}[\%] = 100 \cdot \frac{1}{N_{\text{steps}}} \sum_{i=1}^{N_{\text{steps}}} \frac{|F_i^{\text{EXP}} - F_i^{\text{SIM}}|}{|F_{N_{\text{steps}}}^{\text{EXP}}|} \quad (15a)$$

$$\Delta F_{\text{tot}}^{\text{SIM-HOM}}[\%] = 100 \cdot \frac{1}{N_{\text{steps}}} \sum_{i=1}^{N_{\text{steps}}} \frac{|F_i^{\text{SIM}} - F_i^{\text{HOM}}|}{|F_{N_{\text{steps}}}^{\text{SIM}}|} \quad (15b)$$

304 where  $N_{\text{steps}}$  is the number of displacement steps,  $N_n$  is the number of key nodes in the structure,  
 305  $F_i$  is the force in the displacement step  $i$ .

306 Similarly, the normalized displacement differences are defined by:

$$\Delta u_{\text{tot}}^{\text{EXP-SIM}}[\%] = 100 \cdot \frac{1}{N_{\text{steps}}} \frac{1}{N_n} \sum_{i=1}^{N_{\text{steps}}} \sum_{j=1}^{N_n} \frac{|\mathbf{u}_{i,j}^{\text{EXP}} - \mathbf{u}_{i,j}^{\text{SIM}}|}{|\mathbf{u}_{N_{\text{steps}},j}^{\text{EXP}}|} \quad (16a)$$

$$\Delta u_{\text{tot}}^{\text{SIM-HOM}}[\%] = 100 \cdot \frac{1}{N_{\text{steps}}} \frac{1}{N_n} \sum_{i=1}^{N_{\text{steps}}} \sum_{j=1}^{N_n} \frac{|\mathbf{u}_{i,j}^{\text{SIM}} - \mathbf{u}_{i,j}^{\text{HOM}}|}{|\mathbf{u}_{N_{\text{steps}},j}^{\text{SIM}}|} \quad (16b)$$

307 where  $\mathbf{u}_{i,j}$  denotes the displacement vector of the key node  $j$  in the displacement step  $i$ .

308 To allow for a direct comparison between experimental and simulated results, the coordinate  
 309 systems in which they are described must be identical. Therefore, a 3D rigid body transformation  
 310 is applied to align the experimental data with the simulation coordinate system. This is achieved

311 by matching the experimental and simulated point clouds of the outer surfaces that are visible  
 312 in the DIC cameras, in the reference (unloaded) configuration, using the iterative closest point  
 313 algorithm [48], implemented via MATLAB's *pcregistericp* function. Then, since experimental  
 314 DIC points and the simulation nodes do not perfectly align, the DIC data is interpolated at the po-  
 315 sitions of the FE nodes using their local barycentric coordinates within the triangular faces on the  
 316 outer surfaces of the simulation elements [49, 50]. Even after transformation and interpolation,  
 317 initial positional differences may exist. This error is quantified using average initial positional  
 318 difference  $\Delta_0^{\text{avg}}$ , defined as:

$$\Delta_0^{\text{avg}} = \frac{1}{N_n} \sum_{j=1}^{N_n} |\mathbf{x}_{0,j}^{\text{EXP}} - \mathbf{x}_{0,j}^{\text{SIM}}| \quad (17)$$

319 where  $\mathbf{x}_{0,j}$  denotes the position vector of the key node  $j$  in the initial configuration step.

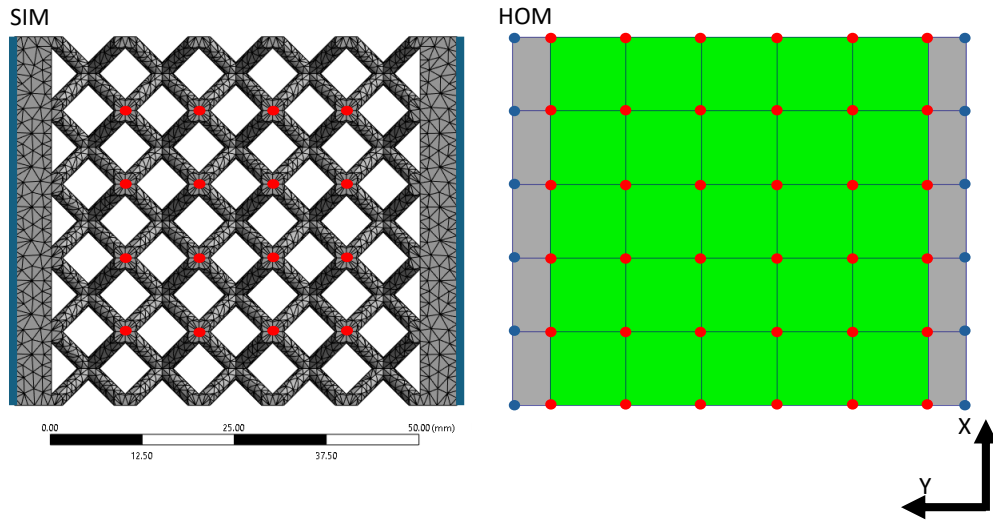


Figure 5: FE simulation boundary conditions of a lattice structure composed of cubic unit cells subjected to compressive loading. SIM is the full-geometry simulation that represents the lattice structures used in the experiments (EXP), and HOM is the homogenized simulation. In the homogenized model, the green elements represent the homogenized equivalent material, whereas the grey elements represent the solid plates composed of the same constituent material. Displacements in the  $Y$  direction, marked in blue, were prescribed to the nodes located on the  $\pm Y$  boundaries of each model, while the same nodes were fully constrained in the  $X$  and  $Z$  directions. The key nodes for comparison between the experimental, simulation, and homogenization results are marked with red dots.

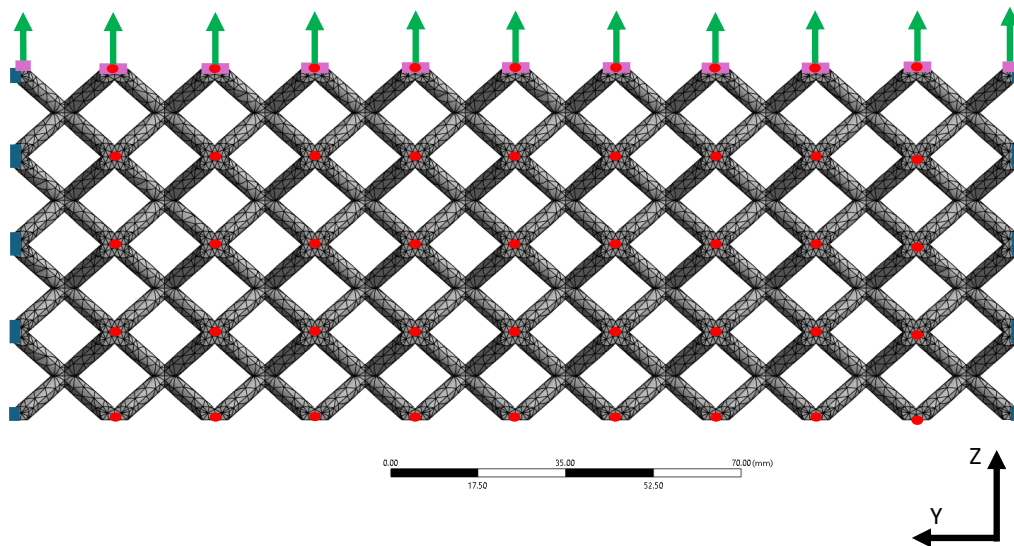


Figure 6: FE simulation model of lattice beam structure composed of orthotropic unit cells. Distributed load, illustrated by green arrows, is applied to nodes on the upper surface, marked in pink, while the nodes on the sides, marked in blue, are fixed. The key nodes for comparison with the homogenized simulation are marked with red dots.

320 **3. Results**

321 *3.1. Lattice structure beam diameters*

322 **Table 1** presents the values of the lattice structures’ beam diameters, as computed using  
 323 the method described in [subsection 2.3](#). The measured density of the printed TPU material is  
 324  $1.07 \text{ g/cm}^3$  [39], compared to the manufacturer’s declared value of  $0.95 \text{ g/cm}^3$ . Notably, the  
 325 dimensions of the 3D-printed specimens differ from those of their CAD models. For simplicity  
 326 of reading, the different unit cells and lattice structures are referred to by their nominal beam  
 327 diameters, even though the FE simulations were conducted using the actual dimensions of the  
 328 printed models.

Table 1: Nominal and measured beam diameters for printed lattice structures.

Measured mass [g]	Nominal diameter [mm]	Printed diameter [mm]
40.44	2.20	1.54
46.11	2.50	1.81
52.79	2.80	2.13
61.23	3.10	2.52

329 *3.2. Homogenization of unit cells*

330 As a compromise between the increased accuracy and elapsed times in unit cells FE simula-  
 331 tions, we chose to use a mesh element size of  $1 \text{ mm}$  for all unit cells, as illustrated in [Figure 2](#).  
 332 The number of elements and nodes is described in [Table 2](#).

Table 2: Number of elements and nodes in FE mesh for unit cells with different symmetries and beam diameters.

Unit cell symmetry	D [mm]	No. Elements [-]	No. Nodes [-]
Cubic	2.2	2926	5479
Cubic	2.5	2786	5142
Cubic	2.8	2814	5108
Cubic	3.1	2757	5005
Orthotropic	3.5	7718	13071

333 FE simulation results for uniaxial stretch and shear strain applied to cubic unit cells with  
 334 varying beam diameters, along with the corresponding stress predictions from the fitted Fung  
 335 model, are presented in [Figure 7](#) and summarized in [Table 3](#). FE simulation results for uniaxial  
 336 stretch and shear strain applied to the orthotropic unit cell at different directions, along with  
 337 the corresponding stress predictions from the fitted Fung model, are presented in [Figure 8](#) and  
 338 summarized in [Table 4](#).

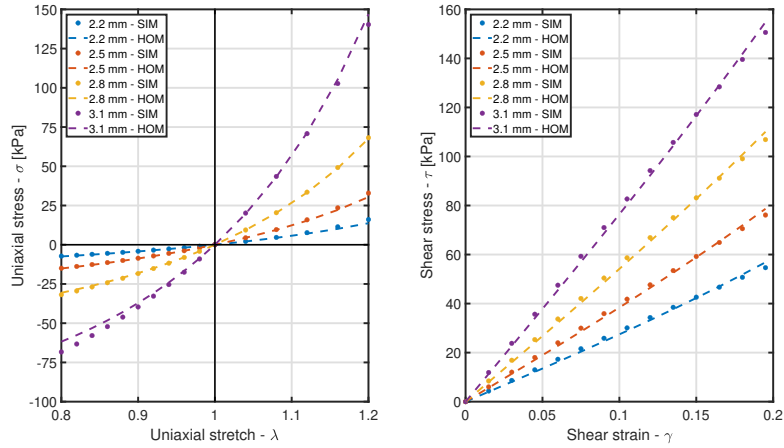


Figure 7: A comparison of stress responses from FE simulations and a homogenized model is presented for cubic unit cells with various beam diameters subjected to uniaxial tension and compression (left), as well as simple shear (right). The stresses obtained from FE simulations are represented by solid dots, and the Fung model fitted values are indicated by a dashed line.

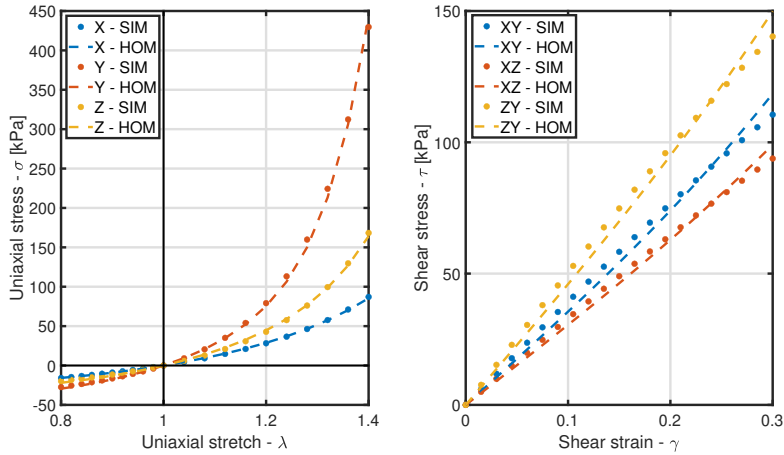


Figure 8: A comparison of the stress responses from FE simulations and a homogenized model is presented for an orthotropic unit cell subjected to uniaxial tension and compression (left), as well as simple shear (right) in the three principal directions. The stresses obtained from FE simulations are represented by solid dots, and the Fung model fitted values are indicated by a dashed line.

Table 3: Summary of Fung model fitting results, including the fitted model parameters and the coefficients of determination ( $R^2$ ), for cubic unit cells with various beam diameters ( $D$ ).

$D$ [mm]	$R^2$ [-]	$E$ [kPa]	$\nu$ [-]	$G$ [kPa]	$\kappa$ [kPa]	$c_0$ [kPa]
2.2	0.9964	56	0.454	269	0	162
2.5	0.9975	113	0.450	377	0	329
2.8	0.9980	230	0.447	533	0	687
3.1	0.9982	469	0.425	754	0	1411

Table 4: Summary of Fung model fitting results for the orthotropic unit cell, including the fitted model parameters and the coefficients of determination ( $R^2$ ).

$R^2$ [-]	$E_{11}$ [kPa]	$E_{22}$ [kPa]	$E_{33}$ [kPa]	$G_{12}$ [kPa]	$G_{23}$ [kPa]	$G_{31}$ [kPa]	$\nu_{12}$ [-]	$\nu_{23}$ [-]	$\nu_{31}$ [-]	$\kappa$ [kPa]	$c_0$ [kPa]
0.9990	105.0	237.3	152.1	350.1	454.8	301.7	0.273	0.675	0.483	0.0	$1.78 \times 10^8$

339 The dependency of the cubic Fung constitutive model parameters ( $E, G, \nu$ , and  $c_0$ ) on the  
340 beam diameter, based on the results listed in Table 3, was analyzed and fitted using second-order  
341 polynomial functions, as shown in Figure 9. These fitting results can be used to estimate the  
342 Fung cubic constitutive model parameters for other values of beam diameters.

343 Although this research focuses on BC lattice structures, a wide variety of other topologies  
344 exist (see, for example, [51]). To evaluate the generalizability of our methodology, we examined  
345 the fitting of the Fung constitutive model to two additional lattice topologies: cube and octagonal  
346 unit cells. Each unit cell had a size of  $10 \times 10 \times 10 \text{ mm}^3$ , with beam diameters of  $3 \text{ mm}$  for the cube  
347 and  $1.5 \text{ mm}$  for the octagonal unit cell. We employed the same PBCs outlined in subsection 2.2  
348 and constitutive model described in subsection 2.1. Figure 10 presents the resulting uniaxial and  
349 shear stress-strain relations, along with the corresponding stress predictions derived from the  
350 fitted Fung model.

### 351 3.3. Equilibrium force from exponential decay fitting

352 The relaxation behavior of the lattice structure under constant displacement was analyzed  
353 using the exponential decay model described in subsection 2.3. A two-term exponential decay  
354 provided a good fit, and the equilibrium force ( $F_\infty$ ) for each displacement step was determined  
355 by fitting the measured force relaxation data to (14) with  $N = 2$ . Figure 11 illustrates exem-  
356 plary fitting results for a representative displacement step of the  $D = 2.5 \text{ mm}$  lattice structure.  
357 The measured force data points are plotted alongside the fitted curves, demonstrating excellent  
358 agreement. Similar results were observed for all other displacement steps across all lattice struc-  
359 tures.

### 360 3.4. Cubic lattice structures: experimental and simulation results

361 We compared the results obtained from the experiments, simulation of the full lattice geome-  
362 try, and simulation of the homogenized model. The simulation times of the full-geometry lattice  
363 structures were approximately 45 minutes, while the homogenized simulations took only a few

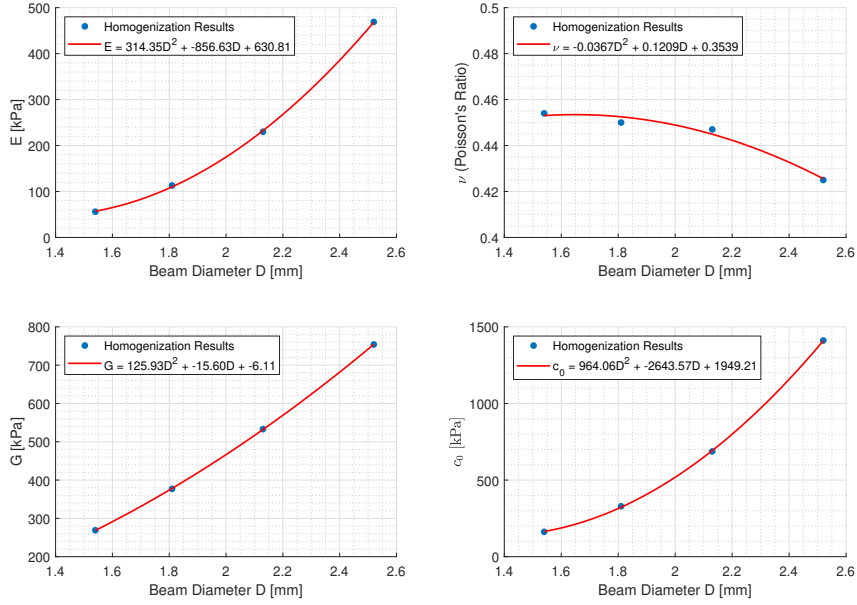


Figure 9: Fung model parameters  $E$ ,  $G$ ,  $\nu$ ,  $c_0$  as a function of beam diameter ( $D$ ) for a BC cubic unit cell. The fitting equation for each curve is also shown within the figure.

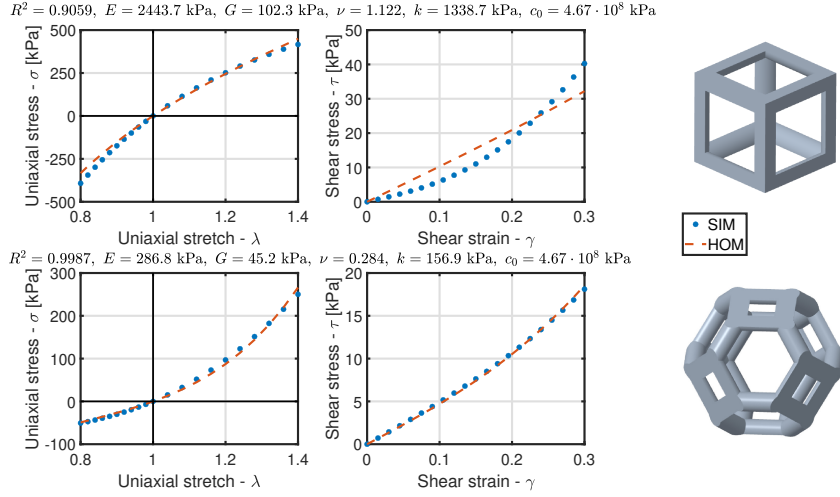


Figure 10: Homogenization analysis for cube (upper) and octagonal (lower) unit cells. The figure illustrates the comparison between simulation and homogenization results in uniaxial and shear deformations. The fitted Fung model parameters and the coefficient of determination ( $R^2$ ) are shown for each topology.

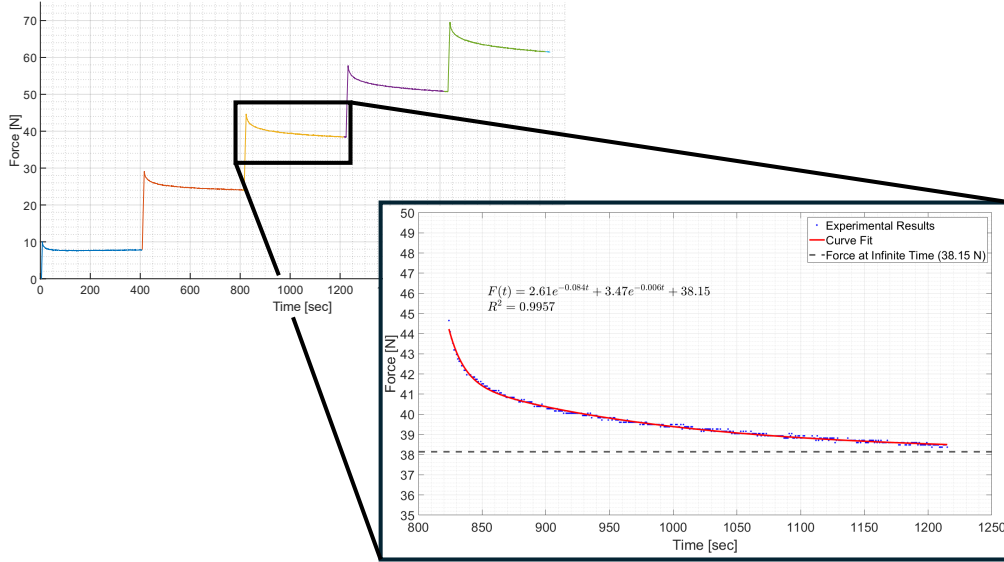


Figure 11: Force measurements of the  $D = 2.5 \text{ mm}$  lattice structure during compression test, demonstrating stress relaxation. The inset shows a zoomed-in view of the relaxation behavior observed during the third displacement step, alongside its fitted two-term exponential decay function described in (14).

seconds. The comparison included the reaction forces and the displacements of key nodes, as described in subsection 2.4. The compressive reaction forces are shown in Figure 12, comparing experimental results with the corresponding simulations, and homogenized model predictions with simulations, across various beam diameters.

During the experiments, we observed that the displacements measured using DIC at the boundaries of the structures differed slightly from those specified to the testing machine. Therefore, the displacement values prescribed in the SIM simulation were adjusted to match the experimental ones, as can be seen in Figure 12.

A representative full-field displacement map, comparing the experimental results obtained using DIC with the corresponding full-geometry simulation, is shown in Figure 13. Similarly, Figure 14 illustrates a comparison between the full-geometry and homogenized simulations. Furthermore, Figure 15 and Figure 16 depict the relative differences in the displacements of the key nodes at each step of structure compression, comparing experimental versus simulation and simulation versus homogenization results, respectively.

The average initial positional difference  $\Delta_0^{\text{avg}}$ , as well as the relative differences in the displacements ( $\Delta u_{\text{tot}}$ ) and force ( $\Delta F_{\text{tot}}$ ) are summarized in Table 5.

### 3.5. Simulation of beam with orthotropic unit cells

As a demonstrative case with multiple deformation modes, we compared the homogenization accuracy for a beam with orthotropic unit cells subjected to a distributed load that caused bending. As detailed in subsection 2.4, the displacements were evaluated at key nodes, as shown in Figure 6. The displacement magnitudes across the structure for the full-geometry and the homogenized simulations are shown in Figure 17 for the last simulation step. Moreover, the relative differences in the displacements of the key nodes at each force step are shown in Figure 18. The

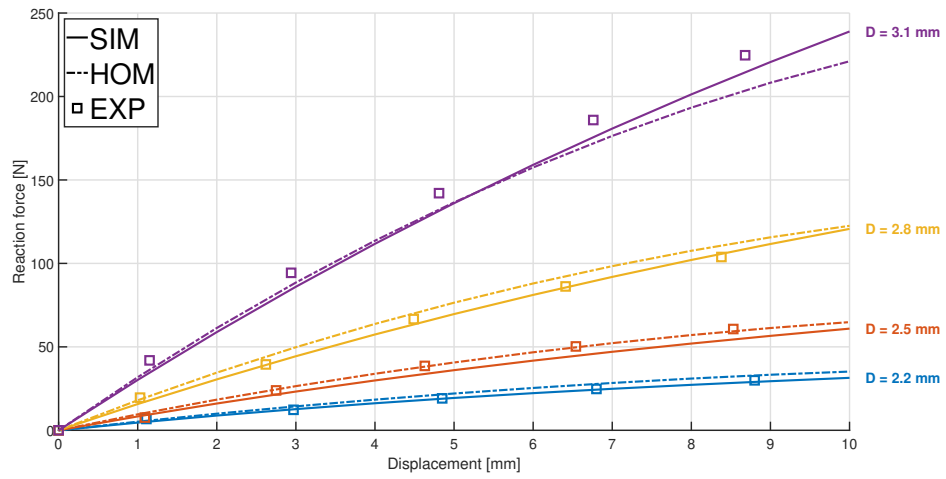


Figure 12: Comparison of compressive force-displacement results between FE full-geometry simulation (SIM), corresponding homogenized model (HOM), and experiments (EXP), for four lattice structures with varying beam diameters (D).

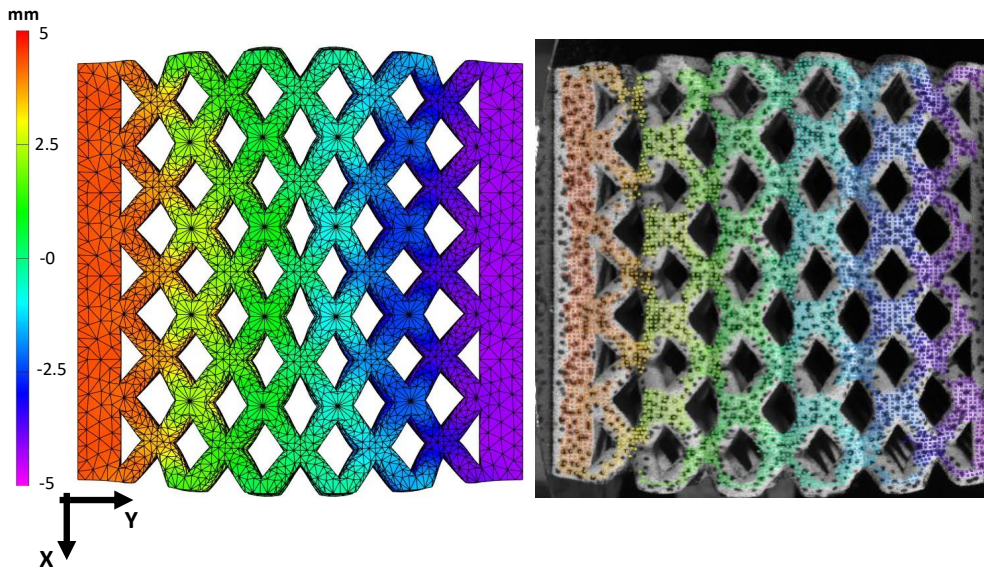


Figure 13: Full-field displacement in the Y direction for the  $D = 3.1$  mm lattice structure at maximum compression, comparing the FE simulation results (left), and experimental results obtained using DIC (right).

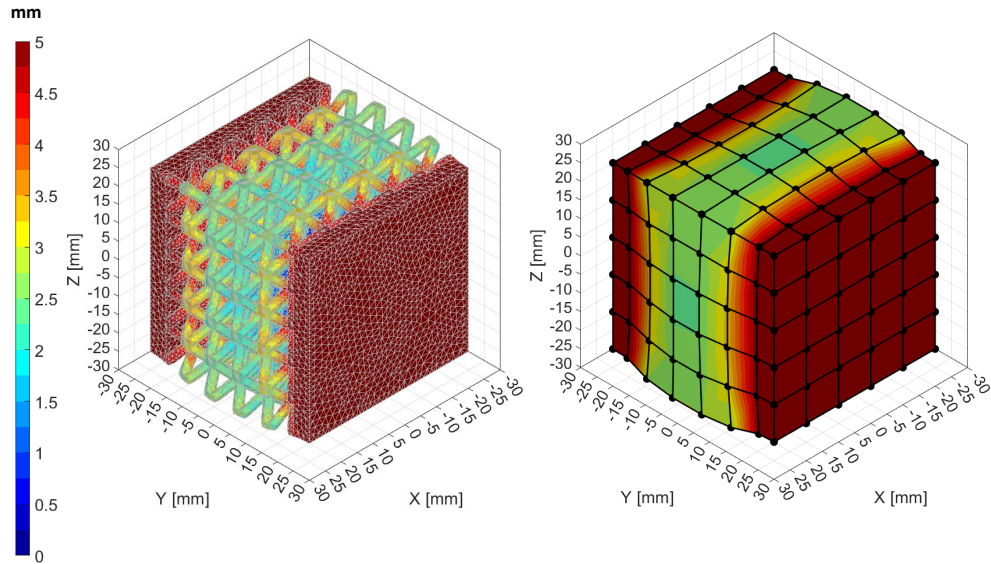


Figure 14: Displacement magnitude maps for the  $D = 3.1 \text{ mm}$  lattice structure at maximum compression, comparing the FE simulation results obtained for the full-geometry model (left), and the homogenized model (right).

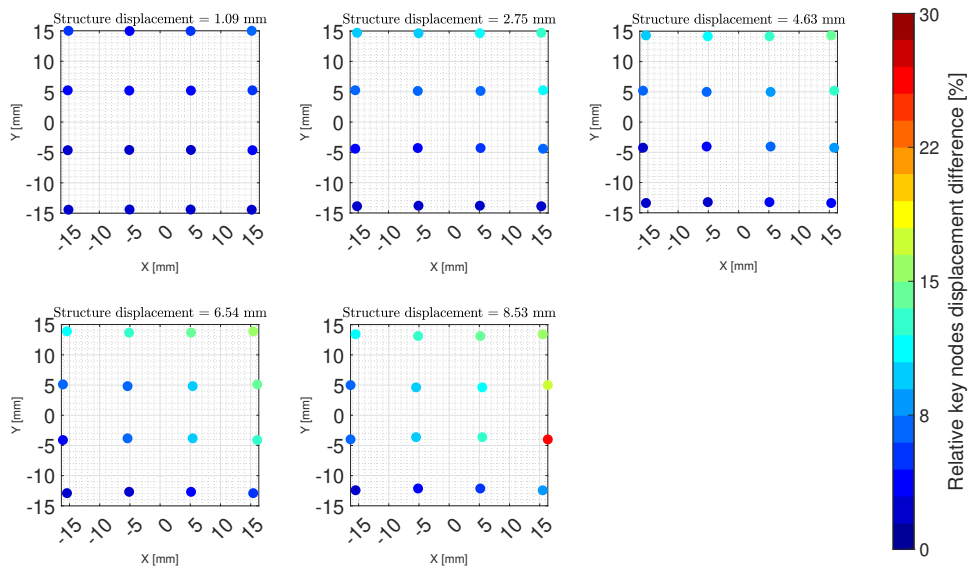


Figure 15: Relative difference in displacements between experimental and FE full-geometry simulations, at the key nodes (see Figure 5) of the  $D = 2.5 \text{ mm}$  lattice structure, at each structure compression step.

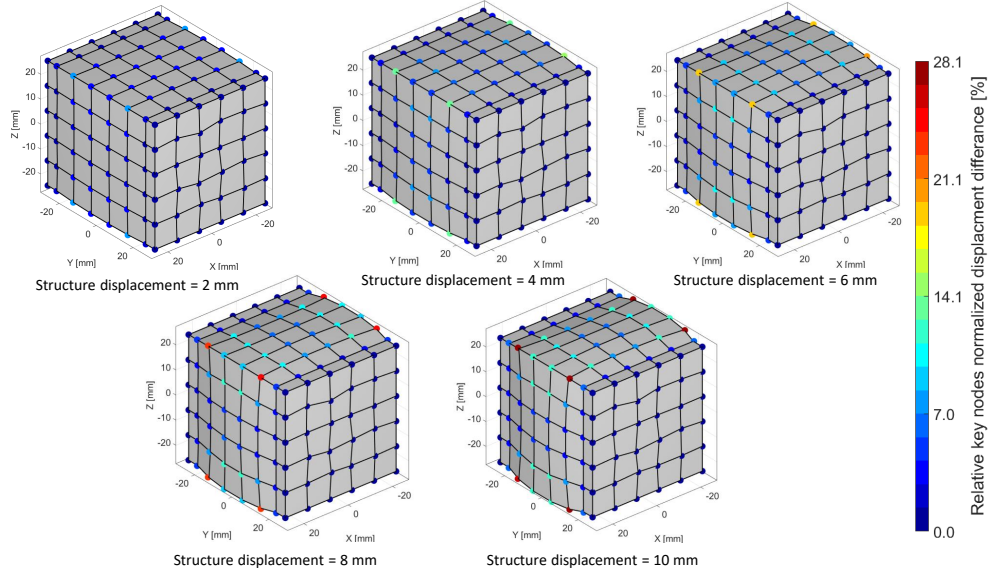


Figure 16: Relative difference in displacements between FE full-geometry simulation and homogenized simulation, at the key nodes, for the  $D = 2.2 \text{ mm}$  lattice structure at multiple structure displacement steps. It can be seen that the key nodes at the edges of the structure exhibit larger displacement differences than the nodes in the center of the structure.

Table 5: Comparison of displacement and force differences between experimental (EXP), full-geometry simulation (SIM), and homogenized simulation (HOM) results, for various lattice structure beam diameters ( $D$ ).

Nominal beam diameter $D$ [mm]	Initial average position error $\Delta_0^{\text{avg}}$ [mm] Eq. (17)	Displacement difference $\Delta u_{\text{tot}}^{\text{EXP-SIM}}$ [%] Eq. (16a)	Force difference $\Delta F_{\text{tot}}^{\text{EXP-SIM}}$ [%] Eq. (15a)	Displacement difference $\Delta u_{\text{tot}}^{\text{SIM-HOM}}$ [%] Eq. (16b)	Force difference $\Delta F_{\text{tot}}^{\text{SIM-HOM}}$ [%] Eq. (15b)
2.2	0.3	8.1	2.3	5.6	8.3
2.5	0.3	7.3	6.4	4.0	6.4
2.8	0.2	7.1	2.4	3.5	4.1
3.1	0.3	6.3	4.2	3.1	2.7

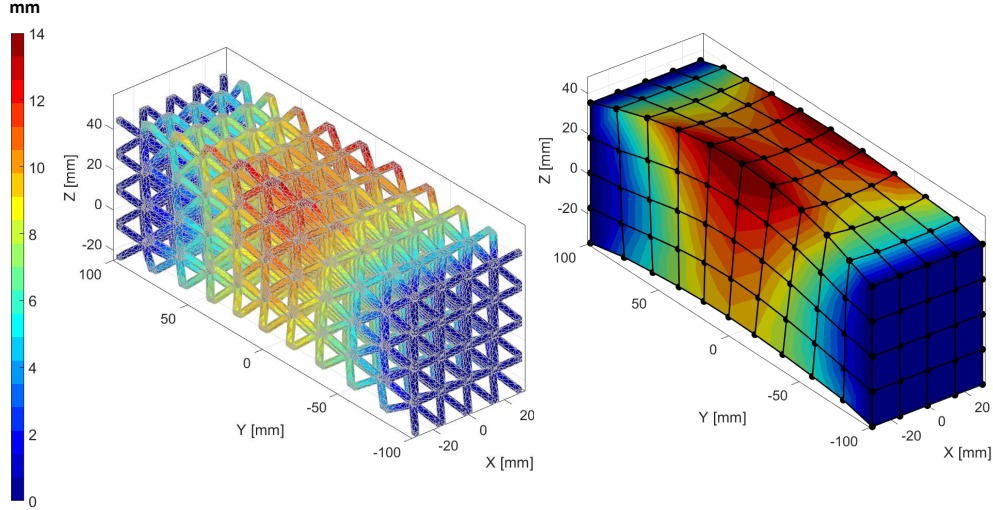


Figure 17: Displacement magnitude results for the full-geometry simulation (left) and homogenized simulation (right) of the beam with orthotropic unit cells. Results are shown for the last force step (300 N).

387 total displacement relative difference between the full-geometry and homogenized simulations is  
 388  $\Delta u_{\text{tot}}^{\text{SIM-HOM}} = 7.4\%$ .

#### 389 4. Discussion

390 This study presents a numerical homogenization framework for lattice structures, which cap-  
 391 tures their orthotropic nonlinear elastic response under tension, compression, and shear loadings.  
 392 Replacing the lattice structures with homogenized solid elements of equivalent properties sub-  
 393 stantially reduces computation time, with only a slight compromise in simulation accuracy. This  
 394 enables practical analysis of large structures with numerous unit cells, facilitating rapid iterative  
 395 design optimization workflows.

396 Since this study involved experimental validation, all the FE simulations used the material  
 397 parameters of the TPU powder, Flexa Bright™ 3D printed through SLS, which was charac-  
 398 terized in a previous study [39]. In the current study, we modeled the constituent material as  
 399 isotropic linear elastic, neglecting the observed stiffness variations due to printing orientation,  
 400 differences between tension and compression, as well as viscoelastic effects [39]. This deliberate  
 401 compromise was made to prioritize the simplicity of the simulations and keep the focus on the  
 402 homogenization procedure.

403 We fabricated BC cubic lattice structures with varying beam diameters. The measured di-  
 404 mensions of the beam diameters differed substantially from the nominal dimensions specified in  
 405 the CAD models, as summarized in Table 1. This discrepancy is likely due to the specific condi-  
 406 tions and parameters of the 3D printing process. As previously reported for other SLS printers,  
 407 factors such as temperature gradients in the build chamber and differential shrinkage between  
 408 adjacent layers can contribute to dimensional deviations [52, 53, 54]. Although it is possible

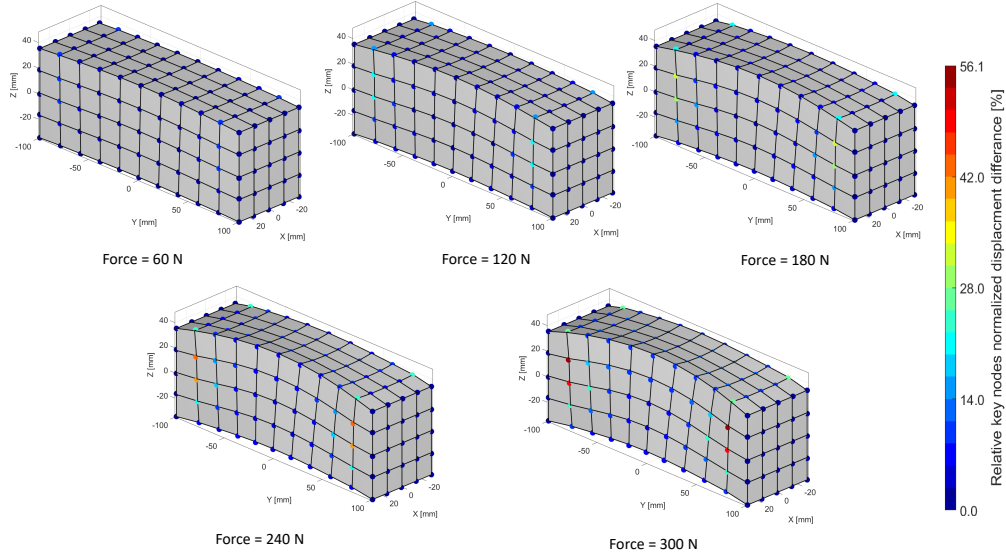


Figure 18: Relative displacement differences obtained from comparing full-geometry and homogenized simulations of the beam with orthotropic unit cells, shown for each force step.

409 to reduce these artifacts by optimizing the printing parameters and implementing advances in  
 410 SLS technology [55], our study did not focus on minimizing the differences between the CAD  
 411 models and the printed samples. Instead, we measured the dimensions of the fabricated samples,  
 412 assuming a homogeneous beam diameter within each structure, and ensured this homogeneity  
 413 by orienting the structures  $45^\circ$  relative to the build platform, as shown in Figure 4a.

414 During the compression experiments on the BC lattice structures, the reaction forces and  
 415 full-field displacements were measured. Although equal displacements were applied to both  
 416 compression platens, the DIC results revealed unexpected asymmetry and displacements that  
 417 deviated from those applied to the platens. This difference was attributed to incomplete bonding  
 418 between the printed plates and aluminum adapters, resulting in a gradual closure of the gap during  
 419 loading. As a result, the actual displacements of the structure's solid plates deviated from those  
 420 applied by the machine. To allow a proper comparison between experimental and simulation  
 421 results, we prescribed the same displacement data measured via DIC as boundary conditions to  
 422 the solid plates in the corresponding simulations.

423 In the FE simulations of the unit cells that were conducted as part of the homogenization  
 424 process, the cubic and orthotropic BC unit cells exhibited notable nonlinear responses when  
 425 subjected to uniaxial tension and compression, while the responses to simple shear were nearly  
 426 linear, as shown in Figure 7 and Figure 8. Capturing the homogenized response required a hy-  
 427 perelastic orthotropic constitutive model to accurately represent the stress-strain relationships of  
 428 all deformation modes. The results presented in subsection 3.2 confirm that the Fung hyperelas-  
 429 tic compressible orthotropic model is well suited for this task, with  $R^2$  values greater than 0.99  
 430 for all fittings. The Fung model exhibited good fitting also to the cube and octagonal unit cells  
 431 (see Figure 10), except for the shear response of the cube unit cell, where the fit was less good.  
 432 This reduced fit quality is attributed to the alignment of all beams in the cube unit cell with the

433 load direction, as opposed to the octagonal and BC unit cells that feature diagonal beams. The  
434 perpendicular beam orientation to the shear plane induced a highly nonlinear response that is not  
435 captured as well by the Fung model, as evident by its overall fitting  $R^2$  value of 0.9, compared to  
436 the  $R^2 > 0.99$  for the octagonal unit cell.

437 The relations between the beam diameters of the unit cells and parameters of the Fung con-  
438 stitutive model (i.e.,  $E$ ,  $G$ ,  $\nu$ , and  $c_0$ ) exhibit nonlinear trends, as illustrated in Figure 9. The  
439 fitted polynomial functions describing these relations facilitate the estimation of constitutive pa-  
440 rameters for other beam diameters, thereby supporting the design of structures with targeted  
441 mechanical properties.

442 The comparison of reaction forces and displacements at key nodes among the experimental  
443 measurements, full-geometry simulations, and homogenized models revealed strong agreement  
444 in both the reaction force and the nodal displacements across all structures, as shown in Fig-  
445 ures 12-16 and summarized in Table 5. Notably, the homogenized simulations required only  
446 a small fraction of the computational time satisfactorily reproducing the mechanical responses,  
447 with relative errors ranging from 2.3% to 8.1%. Assessment of the goodness of fit between  
448 the simulated and experimental data indicates that the simplified, isotropic linear elastic mate-  
449 rial model yields accurate results for all tested structures, highlighting the dominant influence  
450 of unit cell geometry over the precise description of constituent material parameters. However,  
451 it is plausible that for structures with larger solid-to-void volume ratios or for cases involving  
452 larger deformations, more advanced material models may be necessary to properly capture the  
453 mechanical behavior of the TPU constituent. Such models could include those accounting for  
454 orientation dependence [56], tension-compression asymmetry [57], and nonlinear elasticity [58],  
455 effects that were observed in the tested material but neglected in the present simulations [39].  
456 Future studies should investigate the potential impact of these more sophisticated models on the  
457 accuracy of simulations.

458 When comparing the nodal displacements between homogenization and full-geometry sim-  
459 ulations, the largest discrepancies occur at the outer boundaries of the lattice structure. This  
460 can be attributed to the reduced representativeness of the unit cell in these regions, particularly  
461 in terms of the PBCs used for homogenization. The small differences observed in the reaction  
462 forces suggest that the homogenization method effectively captures the stiffness of the structures.

463 The results of the beam with orthotropic unit cells (Figure 17 and Figure 18) demonstrate  
464 that the homogenization method is effective also for lattice structures with orthotropic unit cells  
465 subjected to combined deformation modes, such as bending caused by a distributed load across  
466 a thick beam-like structure.

## 467 5. Conclusions and Future Work

468 The developed homogenization approach successfully captured the nonlinear, orthotropic  
469 response of lattice structures with thick beams. The Fung compressible orthotropic model ac-  
470 curately represented the stress-strain behavior under multiple loading modes. The homogenized  
471 models demonstrated strong agreement with full-geometry simulations in terms of both reac-  
472 tion forces and displacement fields. The largest displacement discrepancies occurred at structure  
473 boundaries, where the assumptions of periodicity and unit cell representativeness become less  
474 valid. The substitution of detailed lattice geometries with homogenized solids significantly re-  
475 duced computational costs, enabling efficient simulation of large-scale structures. Although the  
476 constituent material was modeled using a simplified isotropic linear elastic formulation, it yielded  
477 satisfactory accuracy.

478 Various future research directions can stem from the current study. First, this study focused  
479 on BC unit cells and demonstrated that the Fung model may also be suitable for a cube and oc-  
480 tagonal unit cells. Further investigation into other topologies and types of lattice structures (e.g.,  
481 as in [37, 59, 51, 60, 61]) could expand the method's applicability. Second, this study employed  
482 the Fung model for homogenization, which provided satisfactory results for the investigated unit  
483 cells. However, it is possible that other topologies may exhibit responses that cannot be fitted  
484 well with the Fung model. Therefore, future research could explore the use of machine learning-  
485 based techniques for discovering suitable material models, as previously suggested by various  
486 researchers (e.g., [62, 63, 64]).

487 Furthermore, in this study, we used the equilibrium force and excluded data collected during  
488 stress relaxation when fitting the hyperelastic effective response. Future research could incorpo-  
489 rate viscoelastic models to account for the observed time-dependent responses [65]. Addition-  
490 ally, the proposed framework could be expanded to include responses to dynamic impact loads  
491 and vibrations [66]. Future work could also integrate the proposed homogenization method  
492 into iterative design frameworks, which are currently mostly limited to linear elasticity [67, 11].  
493 Moreover, future research should apply this framework to more complex scenarios, where lattice  
494 unit cells will occupy the geometries of actual (non-rectangular) parts and be subjected to various  
495 loading conditions. This integration could enable the optimization of lattice structures based on  
496 user-defined performance criteria, particularly in applications that necessitate softer structures,  
497 such as those interfacing with soft tissues (e.g., [3, 5, 7, 9]).

#### 498 **Acknowledgements**

499 This work was supported by PTC grant no. 1021190 and the Technion Additive Manufactur-  
500 ing Center (TAMC) grant no. 86638407. The funders had no role in the study design, the data  
501 collection and analysis, the decision to publish, or the preparation of the manuscript.

#### 502 **Declaration of Interest statement**

503 The authors declare that they have no known competing financial interests or personal rela-  
504 tionships that could have appeared to influence the work reported in this paper.

#### 505 **CRedit authorship contribution statement**

506 **Dror Raf:** Writing – original draft, Writing – review & editing, Data curation, Resources,  
507 Conceptualization, Visualization, Software, Methodology, Investigation, Formal analysis. **Itay**  
508 **Magen:** Investigation, Methodology, Validation, Software. **Amit Ashkenazi:** Investigation,  
509 Methodology, Software. **Lee Jordan:** Methodology, Resources, Project administration. **Dana**  
510 **Solav:** Writing – review & editing, Conceptualization, Methodology, Supervision, Project ad-  
511 ministration, Funding acquisition.

#### 512 **References**

513 [1] K. V. Wong, A. Hernandez, A Review of Additive Manufacturing, ISRN Mechanical  
514 Engineering 2012 (2012) 1–10. doi:[10.5402/2012/208760](https://doi.org/10.5402/2012/208760).

- 515 [2] G. Dong, Y. Tang, Y. F. Zhao, A survey of modeling of lattice structures fabricated by  
516 additive manufacturing, *Journal of Mechanical Design, Transactions of the ASME* 139  
517 (2017) 1–13. doi:10.1115/1.4037305.
- 518 [3] G. Dong, D. Tessier, Y. F. Zhao, Design of shoe soles using lattice structures fabricated  
519 by additive manufacturing, *Proceedings of the International Conference on Engineering  
520 Design, ICED 2019-Augus* (2019) 719–728. doi:10.1017/dsi.2019.76.
- 521 [4] O. Ulerich, S. Cananau, D. A. Prisecaru, M. Mărgăritescu, C.-S. Negrea, Design of Cus-  
522 tomized Shoe Soles Using Lattice Structures Fabricated by Additive Manufacturing, in:  
523 A. Burduk, A. D. L. Batako, J. Machado, R. Wyczółkowski, E. Dostatni, I. Rojek (Eds.), *Int-  
524 telligent Systems in Production Engineering and Maintenance III*, Springer Nature Switzer-  
525 land, Cham, 2024, pp. 209–228. doi:10.1007/978-3-031-44282-7\_17.
- 526 [5] Y. Sterman, D. Solav, N. Rosen, E. Saffuri, L. Shmilov Zaritsky, Custom orthotic insoles  
527 with gradual variable stiffness using 3D printed spacer technique, *Virtual and Physical  
528 Prototyping* 19 (2024) e2336151. URL: [https://doi.org/10.1080/17452759.2024.  
529 2336151](https://doi.org/10.1080/17452759.2024.2336151). doi:10.1080/17452759.2024.2336151, publisher: Taylor & Francis \_eprint:  
530 <https://doi.org/10.1080/17452759.2024.2336151>.
- 531 [6] Z. Ma, J. Lin, X. Xu, Z. Ma, L. Tang, C. Sun, D. Li, C. Liu, Y. Zhong, L. Wang,  
532 Design and 3D printing of adjustable modulus porous structures for customized di-  
533 abetic foot insoles, *International Journal of Lightweight Materials and Manufacture*  
534 *2* (2019) 57–63. URL: [https://www.sciencedirect.com/science/article/pii/  
535 S2588840418300477](https://www.sciencedirect.com/science/article/pii/S2588840418300477). doi:10.1016/j.ijlmm.2018.10.003.
- 536 [7] H. M. Herr, K. M. Moerman, D. Solav, B. J. Ranger, R. Steinmeyer, S. L. Ku, C. Dagde-  
537 viren, M. Carney, G. A. Prieto-Gomez, X. Zhang, others, *Quantitative Design and Manu-  
538 facturing Framework for a Biomechanical Interface Contacting a Biological Body Segment*,  
539 2021.
- 540 [8] P. Rai, V. Jankiraman, M. Teacher, R. Velu, S. Anand Kumar, T. Binedell, K. Subburaj,  
541 Design and optimization of a 3D printed prosthetic socket for transtibial amputees, *Materials Today: Proceedings* 70 (2022) 454–464. URL: [https://www.sciencedirect.com/  
542 science/article/pii/S2214785322061818](https://www.sciencedirect.com/science/article/pii/S2214785322061818). doi:10.1016/j.matpr.2022.09.365.
- 543 [9] S. De La Rosa, P. F. Mayuet, J. Ramón, M. Salgueiro, L. Rodríguez-Parada, Design  
544 of Customized TPU Lattice Structures for Additive Manufacturing: Influence on the  
545 Functional Properties in Elastic Products (2021). URL: [https://doi.org/10.3390/  
546 polym13244341](https://doi.org/10.3390/polym13244341). doi:10.3390/polym13244341.
- 547 [10] A. Vigliotti, V. S. Deshpande, D. Pasini, Non linear constitutive models for lattice  
548 materials, *Journal of the Mechanics and Physics of Solids* 64 (2014) 44–60. URL:  
549 <https://linkinghub.elsevier.com/retrieve/pii/S0022509613002238>. doi:10.  
550 1016/j.jmps.2013.10.015.
- 551 [11] G. Savio, A. Curtarello, S. Rosso, R. Meneghello, G. Concheri, Homogeniza-  
552 tion driven design of lightweight structures for additive manufacturing, *International  
553 Journal on Interactive Design and Manufacturing (IJIDeM)* 13 (2019) 263–276.  
554 URL: <http://link.springer.com/10.1007/s12008-019-00543-0>. doi:10.1007/  
555 s12008-019-00543-0.

- 557 [12] G. P. Phlipot, D. M. Kochmann, A quasicontinuum theory for the nonlinear mechanical  
558 response of general periodic truss lattices, *Journal of the Mechanics and Physics of Solids*  
559 124 (2019) 758–780. Publisher: Elsevier.
- 560 [13] L. J. Gibson, M. F. Ashby, G. Schajer, C. Robertson, The mechanics of two-dimensional  
561 cellular materials, *Proceedings of the Royal Society of London. A. Mathematical and Phys-*  
562 *ical Sciences* 382 (1982) 25–42. Publisher: The Royal Society London.
- 563 [14] H. Askes, M. Lombardo, D. C. D. Nguyen, Homogenisation of periodic lattices with  
564 lumped and distributed mass: Beam models, continualisation and stabilisation, *Inter-*  
565 *national Journal of Solids and Structures* 302 (2024) 112988. URL: <https://www.sciencedirect.com/science/article/pii/S0020768324003470>. doi:10.1016/j.  
566 *ijsolstr*.2024.112988.
- 568 [15] L. R. Meza, G. P. Phlipot, C. M. Portela, A. Maggi, L. C. Montemayor, A. Comella, D. M.  
569 Kochmann, J. R. Greer, Reexamining the mechanical property space of three-dimensional  
570 lattice architectures, *Acta Materialia* 140 (2017) 424–432. URL: <https://www.sciencedirect.com/science/article/pii/S1359645417307073>. doi:10.1016/j.  
571 *actamat*.2017.08.052.
- 573 [16] G. De Pasquale, M. Montemurro, A. Catapano, G. Bertolino, L. Revelli, Cellular struc-  
574 tures from additive processes: Design, homogenization and experimental validation, *Proce-*  
575 *dia Structural Integrity* 8 (2018) 75–82. URL: [https://doi.org/10.1016/j.prostr.](https://doi.org/10.1016/j.prostr.2017.12.009)  
576 [2017.12.009](https://doi.org/10.1016/j.prostr.2017.12.009). doi:10.1016/j.prostr.2017.12.009, publisher: Elsevier B.V.
- 577 [17] Y. Tang, Y. Zhou, T. Hoff, M. Garon, Y. F. Zhao, Elastic modulus of 316 stainless steel  
578 lattice structure fabricated via binder jetting process, *Materials Science and Technology*  
579 (United Kingdom) 32 (2016) 648–656. doi:10.1179/1743284715Y.0000000084.
- 580 [18] M. G. Geers, V. G. Kouznetsova, K. Matouš, J. Yvonnet, Homogenization methods and  
581 multiscale modeling: nonlinear problems, *Encyclopedia of computational mechanics sec-*  
582 *ond edition* (2017) 1–34. Publisher: Wiley Online Library.
- 583 [19] S.-I. Park, D. W. Rosen, S.-k. Choi, C. E. Duty, Effective mechanical properties of lattice  
584 material fabricated by material extrusion additive manufacturing, *Additive Manufacturing*  
585 1 (2014) 12–23. Publisher: Elsevier.
- 586 [20] R. Gümrük, R. Mines, Compressive behaviour of stainless steel micro-lattice structures,  
587 *International Journal of Mechanical Sciences* 68 (2013) 125–139. Publisher: Elsevier.
- 588 [21] O. Weeger, Numerical homogenization of second gradient, linear elastic constitutive  
589 models for cubic 3D beam-lattice metamaterials, *International Journal of Solids and*  
590 *Structures* 224 (2021) 111037. URL: [https://www.sciencedirect.com/science/](https://www.sciencedirect.com/science/article/pii/S0020768321001153)  
591 [article/pii/S0020768321001153](https://www.sciencedirect.com/science/article/pii/S0020768321001153). doi:10.1016/j.*ijsolstr*.2021.03.024.
- 592 [22] T. Gärtner, M. Fernández, O. Weeger, Nonlinear multiscale simulation of elastic beam  
593 lattices with anisotropic homogenized constitutive models based on artificial neural net-  
594 works, *Computational Mechanics* 68 (2021) 1111–1130. URL: [https://doi.org/10.](https://doi.org/10.1007/s00466-021-02061-x)  
595 [1007/s00466-021-02061-x](https://doi.org/10.1007/s00466-021-02061-x). doi:10.1007/s00466-021-02061-x.

- 596 [23] Z. Chen, S. Sahoo, M. T. Pérez-Prado, D. Mordehai, The extended scaling laws of  
597 the mechanical properties of additively manufactured body-centered cubic lattice struc-  
598 tures under large compressive strains, *Mechanics of Materials* 196 (2024) 105075. URL:  
599 <https://linkinghub.elsevier.com/retrieve/pii/S0167663624001674>. doi:10.  
600 1016/j.mechmat.2024.105075.
- 601 [24] V. Marchal, T. Shujie, Y. Zhang, N. Labed, F. Peyraut, Multiscale periodic homogeniza-  
602 tion for additive manufacturing of honeycomb lattices, *International Journal of Solids and*  
603 *Structures* 302 (2024) 112974. URL: <https://linkinghub.elsevier.com/retrieve/pii/S0020768324003330>. doi:10.1016/j.ijsolstr.2024.112974.
- 605 [25] V. Jeanneau, C. Combescure, M. François, Homogenized elasticity and domain of linear  
606 elasticity of 2D architected materials, *International Journal of Solids and Struc-*  
607 *tures* 269 (2023) 112185. URL: <https://linkinghub.elsevier.com/retrieve/pii/S0020768323000823>. doi:10.1016/j.ijsolstr.2023.112185.
- 609 [26] S. K. Jalali, M. J. Beigrezaee, D. Misseroni, N. M. Pugno, A modified Gibson-  
610 Ashby model for functionally graded lattice structures, *Mechanics of Materials* 188  
611 (2024) 104822. URL: <https://www.sciencedirect.com/science/article/pii/S0167663623002685>. doi:10.1016/j.mechmat.2023.104822.
- 613 [27] A. Corvi, L. Collini, Combined RVE-Cohesive elements approach to the multi-scale  
614 modelling of FDM 3D-printed components, *Theoretical and Applied Fracture Mechan-*  
615 *ics* 128 (2023) 104140. URL: <https://linkinghub.elsevier.com/retrieve/pii/S0167844223004032>. doi:10.1016/j.tafmec.2023.104140, publisher: Elsevier BV.
- 617 [28] M. S. Anoop, P. Senthil, Homogenisation of elastic properties in FDM components us-  
618 ing microscale RVE numerical analysis, *Journal of the Brazilian Society of Mechan-*  
619 *ical Sciences and Engineering* 41 (2019). URL: <http://link.springer.com/10.1007/s40430-019-2037-8>. doi:10.1007/s40430-019-2037-8, publisher: Springer Science  
620 and Business Media LLC.
- 622 [29] Y. Chen, T. Li, Z. Jia, F. Scarpa, C.-W. Yao, L. Wang, 3D printed hierarchical honeycombs  
623 with shape integrity under large compressive deformations, *Materials & Design* 137 (2018)  
624 226–234. Publisher: Elsevier.
- 625 [30] Y. Jiang, Q. Wang, Highly-stretchable 3D-architected mechanical metamaterials, *Scientific*  
626 *reports* 6 (2016) 34147. Publisher: Nature Publishing Group UK London.
- 627 [31] A. S. Bhuwal, T. Liu, I. Ashcroft, W. Sun, Localization and coalescence of imperfect  
628 planar FCC truss lattice metamaterials under multiaxial loadings, *Mechanics of Materi-*  
629 *als* 160 (2021) 103996. URL: <https://www.sciencedirect.com/science/article/pii/S0167663621002271>. doi:10.1016/j.mechmat.2021.103996.
- 631 [32] L. Beex, R. Peerlings, M. Geers, A quasicontinuum methodology for multiscale analyses  
632 of discrete microstructural models, *International Journal for Numerical Methods in Engi-*  
633 *neering* 87 (2011) 701–718. Publisher: Wiley Online Library.
- 634 [33] H. Liu, J. Lv, An equivalent continuum multiscale formulation for 2D geometrical nonlinear  
635 analysis of lattice truss structure, *Composite Structures* 160 (2017) 335–348. Publisher:  
636 Elsevier.

- 637 [34] A. Damanpack, M. Bodaghi, W. Liao, Experimentally validated multi-scale model-  
638 ing of 3D printed hyper-elastic lattices, *International Journal of Non-Linear Mechan-*  
639 *ics* 108 (2019) 87–110. URL: [https://linkinghub.elsevier.com/retrieve/pii/](https://linkinghub.elsevier.com/retrieve/pii/S0020746218300842)  
640 [S0020746218300842](https://linkinghub.elsevier.com/retrieve/pii/S0020746218300842). doi:10.1016/j.ijnonlinmec.2018.10.008.
- 641 [35] M. Fernández, M. Jamshidian, T. Böhlke, K. Kersting, O. Weeger, Anisotropic hy-  
642 perelastic constitutive models for finite deformations combining material theory and  
643 data-driven approaches with application to cubic lattice metamaterials, *Computa-*  
644 *tional Mechanics* 67 (2021) 653–677. URL: [http://link.springer.com/10.1007/](http://link.springer.com/10.1007/s00466-020-01954-7)  
645 [s00466-020-01954-7](http://link.springer.com/10.1007/s00466-020-01954-7). doi:10.1007/s00466-020-01954-7.
- 646 [36] M. Jamshidian, N. Boddeti, D. Rosen, O. Weeger, Multiscale modelling of soft lat-  
647 tice metamaterials: Micromechanical nonlinear buckling analysis, experimental veri-  
648 fication, and macroscale constitutive behaviour, *International Journal of Mechanical*  
649 *Sciences* 188 (2020) 105956. URL: [https://linkinghub.elsevier.com/retrieve/](https://linkinghub.elsevier.com/retrieve/pii/S002074032032419X)  
650 [pii/S002074032032419X](https://linkinghub.elsevier.com/retrieve/pii/S002074032032419X). doi:10.1016/j.ijmecsci.2020.105956.
- 651 [37] S. Xu, J. Shen, S. Zhou, X. Huang, Y. M. Xie, Design of lattice structures with controlled  
652 anisotropy, *Materials and Design* 93 (2016) 443–447. doi:10.1016/j.matdes.2016.01.  
653 007, publisher: Elsevier.
- 654 [38] M. Shojaee, I. Valizadeh, D. K. Klein, P. Sharifi, O. Weeger, Multiscale modeling of  
655 functionally graded shell lattice metamaterials for additive manufacturing, *Engineering*  
656 *with Computers* 40 (2024) 2019–2036. URL: [https://link.springer.com/10.1007/](https://link.springer.com/10.1007/s00366-023-01906-8)  
657 [s00366-023-01906-8](https://link.springer.com/10.1007/s00366-023-01906-8). doi:10.1007/s00366-023-01906-8.
- 658 [39] D. Raf, I. Magen, L. Jordan, D. Solav, Characterization of the mechanical properties of  
659 TPU fabricated by SLS in different printing orientations, *engrxiv* (2025). doi:[https://](https://doi.org/10.31224/4689)  
660 [doi.org/10.31224/4689](https://doi.org/10.31224/4689).
- 661 [40] Y. C. Fung, K. Fronek, P. Patitucci, Pseudoelasticity of arteries and the choice of its mathe-  
662 matical expression, *American Journal of Physiology-Heart and Circulatory Physiology* 237  
663 (1979) H620–H631. URL: [https://journals.physiology.org/doi/abs/10.1152/](https://journals.physiology.org/doi/abs/10.1152/ajpheart.1979.237.5.h620)  
664 [ajpheart.1979.237.5.h620](https://journals.physiology.org/doi/abs/10.1152/ajpheart.1979.237.5.h620). doi:10.1152/ajpheart.1979.237.5.H620, publisher:  
665 American Physiological Society.
- 666 [41] J. D. Humphrey, *Cardiovascular solid mechanics: cells, tissues, and organs*, Springer Sci-  
667 ence & Business Media, 2013.
- 668 [42] L. Mullins, Softening of rubber by deformation, *Rubber chemistry and technology* 42  
669 (1969) 339–362. doi:10.5254/1.3539210.
- 670 [43] W. Fliigge, *Viscoelasticity*, Blaisdell Publ. Comp., London (1967) 1069–1084. Publisher:  
671 Springer.
- 672 [44] S. Maas, B. Ellis, G. Ateshian, J. Weiss, FEBio: Finite elements for biomechanics, *Journal*  
673 *of Biomechanical Engineering* 134 (2012) 011005. doi:10.1115/1.4005694.
- 674 [45] K. M. Moerman, GIBBON: the geometry and image-based bioengineering add-on, *Journal*  
675 *of Open Source Software* 3 (2018) 506.

- 676 [46] Mikkel Pedersen, ANSYSimport, 2025. URL: [https://www.mathworks.com/](https://www.mathworks.com/matlabcentral/fileexchange/66659-ansysimport)  
677 [matlabcentral/fileexchange/66659-ansysimport](https://www.mathworks.com/matlabcentral/fileexchange/66659-ansysimport).
- 678 [47] K. Radi, F. Allamand, D. M. Kochmann, Deformation tracking of truss lattices  
679 under dynamic loading based on Digital Image Correlation, *Mechanics of Materi-*  
680 *als* 183 (2023) 104658. URL: [https://www.sciencedirect.com/science/article/](https://www.sciencedirect.com/science/article/pii/S0167663623001047)  
681 [pii/S0167663623001047](https://www.sciencedirect.com/science/article/pii/S0167663623001047). doi:10.1016/j.mechmat.2023.104658.
- 682 [48] P. J. Besl, N. D. McKay, Method for registration of 3-D shapes, in: *Sensor fusion IV:*  
683 *control paradigms and data structures*, volume 1611, Spie, 1992, pp. 586–606.
- 684 [49] M. S. Floater, Generalized barycentric coordinates and applications, *Acta Numerica* 24  
685 (2015) 161–214. Publisher: Cambridge University Press.
- 686 [50] Z. Huang, C. Antion, F. Toussaint, Identification for elastoplastic constitutive pa-  
687 rameters of 316L stainless steel lattice structures using finite element model up-  
688 dating and integrated digital image correlation, *Mechanics of Materials* 202  
689 (2025) 105232. URL: [https://www.sciencedirect.com/science/article/pii/](https://www.sciencedirect.com/science/article/pii/S0167663624003247)  
690 [S0167663624003247](https://www.sciencedirect.com/science/article/pii/S0167663624003247). doi:10.1016/j.mechmat.2024.105232.
- 691 [51] A. Parisien, M. S. ElSayed, H. Frei, Mechanoregulation modelling of stretching  
692 versus bending dominated periodic cellular solids, *Materials Today Communica-*  
693 *tions* 33 (2022) 104315. URL: [https://linkinghub.elsevier.com/retrieve/pii/](https://linkinghub.elsevier.com/retrieve/pii/S2352492822011576)  
694 [S2352492822011576](https://linkinghub.elsevier.com/retrieve/pii/S2352492822011576). doi:10.1016/j.mtcomm.2022.104315.
- 695 [52] M. Fahad, N. Hopkinson, Evaluation and comparison of geometrical accuracy of parts  
696 produced by sintering-based additive manufacturing processes, *The International Journal*  
697 *of Advanced Manufacturing Technology* 88 (2017) 3389–3394. Publisher: Springer.
- 698 [53] H.-J. Yang, P.-J. Hwang, S.-H. Lee, A study on shrinkage compensation of the SLS pro-  
699 cess by using the Taguchi method, *International Journal of Machine Tools and Manu-*  
700 *facture* 42 (2002) 1203–1212. URL: [https://linkinghub.elsevier.com/retrieve/](https://linkinghub.elsevier.com/retrieve/pii/S0890695502000706)  
701 [pii/S0890695502000706](https://linkinghub.elsevier.com/retrieve/pii/S0890695502000706). doi:10.1016/S0890-6955(02)00070-6.
- 702 [54] P. Mantada, R. Mendricky, J. Safka, PARAMETERS INFLUENCING THE PRE-  
703 CISION OF VARIOUS 3D PRINTING TECHNOLOGIES, *MM Science Journal*  
704 2017 (2017) 2004–2012. URL: [http://www.mmscience.eu/december-2017.html#](http://www.mmscience.eu/december-2017.html#201776)  
705 [201776](http://www.mmscience.eu/december-2017.html#201776). doi:10.17973/MMSJ.2017\_12\_201776.
- 706 [55] S. Yuan, F. Shen, J. Bai, C. K. Chua, J. Wei, K. Zhou, 3D soft auxetic lattice structures fabri-  
707 cated by selective laser sintering: TPU powder evaluation and process optimization, *Mate-*  
708 *rials and Design* 120 (2017) 317–327. URL: [http://dx.doi.org/10.1016/j.matdes.](http://dx.doi.org/10.1016/j.matdes.2017.01.098)  
709 [2017.01.098](http://dx.doi.org/10.1016/j.matdes.2017.01.098). doi:10.1016/j.matdes.2017.01.098, publisher: Elsevier Ltd.
- 710 [56] X. Guo, E. Wang, H. Yang, W. Zhai, Mechanical characterization and constitutive  
711 modeling of additively-manufactured polymeric materials and lattice structures, *Journal*  
712 *of the Mechanics and Physics of Solids* 189 (2024) 105711. URL: [https://www.](https://www.sciencedirect.com/science/article/pii/S0022509624001777)  
713 [sciencedirect.com/science/article/pii/S0022509624001777](https://www.sciencedirect.com/science/article/pii/S0022509624001777). doi:10.1016/j.  
714 [jmps.2024.105711](https://www.sciencedirect.com/science/article/pii/S0022509624001777).

- 715 [57] K. M. Moerman, C. K. Simms, T. Nagel, Control of tension–compression asym-  
716 metry in Ogden hyperelasticity with application to soft tissue modelling, *Journal of the Mechanical Behavior of Biomedical Materials* 56 (2016) 218–228. URL: <https://linkinghub.elsevier.com/retrieve/pii/S1751616115004452>. doi:10.  
717 1016/j.jmbbm.2015.11.027.  
718  
719
- 720 [58] E. Martín-Sosa, L. Távara, J. Ojeda, A. Estefani, Anisotropic and hyperelastic mechan-  
721 ical response of 3D printed TPU parts, *Progress in Additive Manufacturing* 10 (2025)  
722 5697–5709. URL: <https://doi.org/10.1007/s40964-024-00937-x>. doi:10.1007/  
723 s40964-024-00937-x.
- 724 [59] C. Bonatti, D. Mohr, Mechanical performance of additively-manufactured anisotropic  
725 and isotropic smooth shell-lattice materials: Simulations & experiments, *Journal of the Mechanics and Physics of Solids* 122 (2019) 1–26. URL: [https://www.  
726 sciencedirect.com/science/article/pii/S0022509617309614](https://www.sciencedirect.com/science/article/pii/S0022509617309614). doi:10.1016/j.  
727 jmps.2018.08.022.  
728
- 729 [60] E. Mancini, M. Utzeri, E. Farotti, A. Lattanzi, M. Sasso, DLP printed 3D gy-  
730 roid structure: Mechanical response at meso and macro scale, *Mechanics of Materi-  
731 als* 192 (2024) 104970. URL: [https://www.sciencedirect.com/science/article/  
732 pii/S0167663624000620](https://www.sciencedirect.com/science/article/pii/S0167663624000620). doi:10.1016/j.mechmat.2024.104970.
- 733 [61] M. Vafaefar, K. M. Moerman, T. J. Vaughan, LatticeWorks: An open-source  
734 MATLAB toolbox for nonuniform, gradient and multi-morphology lattice genera-  
735 tion, and analysis, *Materials & Design* 250 (2025) 113564. URL: [https://www.  
736 sciencedirect.com/science/article/pii/S0264127524009390](https://www.sciencedirect.com/science/article/pii/S0264127524009390). doi:10.1016/j.  
737 matdes.2024.113564.
- 738 [62] D. K. Klein, M. Fernández, R. J. Martin, P. Neff, O. Weeger, Polyconvex anisotropic  
739 hyperelasticity with neural networks, *Journal of the Mechanics and Physics of  
740 Solids* 159 (2022) 104703. URL: [https://linkinghub.elsevier.com/retrieve/  
741 pii/S0022509621003215](https://linkinghub.elsevier.com/retrieve/pii/S0022509621003215). doi:10.1016/j.jmps.2021.104703.
- 742 [63] M. Flaschel, S. Kumar, L. De Lorenzis, Unsupervised discovery of interpretable hy-  
743 perelastic constitutive laws, *Computer Methods in Applied Mechanics and Engineer-  
744 ing* 381 (2021) 113852. URL: [https://www.sciencedirect.com/science/article/  
745 pii/S0045782521001894](https://www.sciencedirect.com/science/article/pii/S0045782521001894). doi:10.1016/j.cma.2021.113852.
- 746 [64] O. Z. Tikenogulları, A. K. Açıkan, E. Kuhl, H. Dal, Data-driven hyperelasticity, Part II:  
747 A canonical framework for anisotropic soft biological tissues, *Journal of the Mechanics  
748 and Physics of Solids* 181 (2023) 105453. URL: [https://www.sciencedirect.com/  
749 science/article/pii/S0022509623002570](https://www.sciencedirect.com/science/article/pii/S0022509623002570). doi:10.1016/j.jmps.2023.105453.
- 750 [65] A. Welander, I. Kinnunen, A. Daneryd, J. Hajek, K. Sahu, M. Mousavi, Tailored  
751 energy dissipation with viscoelastic architected materials, *Mechanics of Materi-  
752 als* 201 (2025) 105216. URL: [https://www.sciencedirect.com/science/article/  
753 pii/S0167663624003089](https://www.sciencedirect.com/science/article/pii/S0167663624003089). doi:10.1016/j.mechmat.2024.105216.
- 754 [66] A. Salehian, D. J. Inman, Dynamic analysis of a lattice structure by ho-  
755 mogenization: Experimental validation, *Journal of Sound and Vibration* 316

- 756 (2008) 180–197. URL: [https://www.sciencedirect.com/science/article/pii/](https://www.sciencedirect.com/science/article/pii/S0022460X08001636)  
757 [S0022460X08001636](https://www.sciencedirect.com/science/article/pii/S0022460X08001636). doi:10.1016/j.jsv.2008.02.031.
- 758 [67] X. Zheng, C. , Ta-Te, J. , Xiaoyu, N. , Masanobu, , I. Watanabe, Deep-learning-  
759 based inverse design of three-dimensional architected cellular materials with the target  
760 porosity and stiffness using voxelized Voronoi lattices, Science and Technology of Ad-  
761 vanced Materials 24 (2023) 2157682. URL: [https://doi.org/10.1080/14686996.](https://doi.org/10.1080/14686996.2022.2157682)  
762 [2022.2157682](https://doi.org/10.1080/14686996.2022.2157682). doi:10.1080/14686996.2022.2157682, publisher: Taylor & Francis  
763 \_eprint: <https://doi.org/10.1080/14686996.2022.2157682>.